LASER–PLASMA INTERACTIONS IN NIF-SCALE PLASMAS (HLP5 AND HLP6)

B. MacGowan *M. Casanova** *K. Estabrook* *R. Kirkwood* *J. Moody*

R. Berger *B. Cohen* *S. Glenzer* *W. Kruer* *D. Munro*

*J. Fernandez*** *D. Desenne** *D. Hinkel* *A. Langdon* *L. Powers*

B. Afeyan *D. Dubois*** *D. Kalantar* *B. Lasinski* *H. Rose***

C. Back *A. Dulieu** *R. Kauffman* *D. Montgomery* *C. Rousseaux**

*G. Bonnaud** *R. Turner* *B. Wilde*** *S. Wilks* *E. Williams*

Introduction

The understanding of laser–plasma interactions in ignition-scale inertial confinement fusion (ICF) hohlraum targets is important for the success of the proposed National Ignition Facility (NIF). The success of an indirect-drive ICF ignition experiment depends on the ability to predict and control the history and spatial distribution of the x-radiation produced by the laser beams that are absorbed by the inside of the hohlraum wall. Only by controlling the symmetry of this x-ray drive is it possible to obtain the implosion symmetry in the fusion pellet necessary for ignition.[1] The larger hohlraums and longer time scales required for ignition-scale targets result in the presence of several millimeters of plasma (electron density $n_e \approx 0.1 n_c \approx 10^{21}$ cm^{-3}), through which the 3ω (351-nm) laser beams must propagate before they are absorbed at the hohlraum wall. Hydrodynamic simulations show this plasma to be very uniform [density-gradient scalelength $L_n = n_e(dn_e/dx)^{-1} \approx 2$ mm] and to exhibit low velocity gradients [velocity-gradient scalelength $L_v = c_s(dv/dx)^{-1} > 6$ mm].[2]

The propagation of the beams to the hohlraum wall can be affected by various scattering and laser self-focusing (filamentation) processes within the low-density plasma inside the hohlraum. For example, while traversing such a plasma, the incoming light wave can resonantly decay into a backscattered light wave and either an ion sound wave or an electron plasma wave. The backscattered light wave can beat with the incident light wave at a frequency that pumps the plasma wave; this process can increase the amplitude of the plasma wave, increasing its scattering efficiency. Hence an unstable feedback loop is formed that can cause the amplitudes of the plasma and scattered light waves to grow exponentially on time scales of 0.1 to 10 ps. For scattering from ion sound waves, these parametric scattering instabilities are called stimulated Brillouin scattering (SBS); for scattering from electron plasma waves, they are called stimulated Raman scattering (SRS).[3] Both of these instabilities can lead to undesirable effects, including significant amounts of light reflecting from the plasma or shining directly onto the capsule, spoiling the illumination symmetry.

Another instability that can affect laser beam propagation is beam filamentation,[4] which occurs when individual speckles ("hot spots") within the beam self-focus as a result of refractive index changes caused by changes in the local plasma density produced by the laser field through transverse ponderomotive pressure. This effect can result in a local increase in intensity and eventual beam breakup. Filamentation is of particular concern for NIF hohlraums, because the intensity threshold for filamentation is affected by the length and transverse scale of the hot spot. For a beam smoothed with a random phase plate (RPP), these scales are determined by the beam f/number. The $f/8$ focusing geometry planned for the NIF will have speckles 180 μm long for 351-nm light, contrasting with 50-μm speckles for the $f/4.3$ optics used at the LLNL Nova laser. Calculations indicate that at the expected 2×10^{15} W cm^{-2} irradiance planned for the NIF, a significant fraction of an $f/8$ beam would be above the intensity threshold for filamentation, in the absence of any beam smoothing beyond use of a RPP.[4]

In most laser-produced plasmas, SBS and SRS are limited by plasma inhomogeneity[3]; in the plasmas expected in the NIF hohlraums, however, wave damping,

* Centre D'Etudes de Limeil–Valenton, France

** Los Alamos National Laboratory, Los Alamos, New Mexico

pump depletion, or some other nonlinear saturation mechanism would be the only limitations on instability growth. Some of our interaction experiments in homogeneous low-density plasmas have shown as much as 35% of the incident laser energy backscattered as SBS; in other experiments, SRS reflected fractions as high as 25% have been observed. Although these are extreme cases that represent scattering from plasmas that have less damping of instabilities than we expect in the NIF plasma, they illustrate the potential of parametric instabilities to cause problems. This amount of backscattering would obviously reduce coupling to the hohlraum wall, reducing the x-ray drive and increasing the incident laser energy required to drive a target to ignition. (SRS could cause additional problems, because the process not only transfers energy into backscattered light and electron plasma waves but also produces suprathermal electrons with tens of keV energy. These "hot" electrons can preheat the DT fuel in the capsule, reducing the efficiency of the subsequent implosion.) Significant energy scattering due to instabilities such as SBS and SRS would also make it more difficult to meet the NIF power-balance specification of <8% variation in power between beams, which is needed to meet the symmetry requirements for a high-convergence implosion.[5] SRS and SBS exacerbated by beam filamentation are therefore a concern for indirect-drive ICF, especially in the larger and more uniform plasmas expected in an ignition-scale hohlraum.

The basic design for the NIF hohlraum [Fig. 1(a)] is an Au cylinder about 9 mm long containing a low-Z gas (a mixture of He and H_2). The low-Z gas slows the expansion of the Au hohlraum wall and provides a medium (other than low-density Au ablated from the wall) through which the beams can propagate without significant loss of energy from inverse bremsstrahlung absorption. The current NIF design has two cones of beams (called the inner and outer cones) on each side of the hohlraum. Figure 1(b) shows the history of the NIF laser pulse; Fig. 1(c) shows the density and beam intensity along the beam path for the time of peak calculated SRS and SBS gain (also the time of peak power, 13.5 ns). Figure 1(d) shows the calculated temperature profiles at the same time. The profiles in Figs. 1(c) and (d) represent the beam intensity, electron density, and electron temperature encountered along the inner and outer cone beam paths.

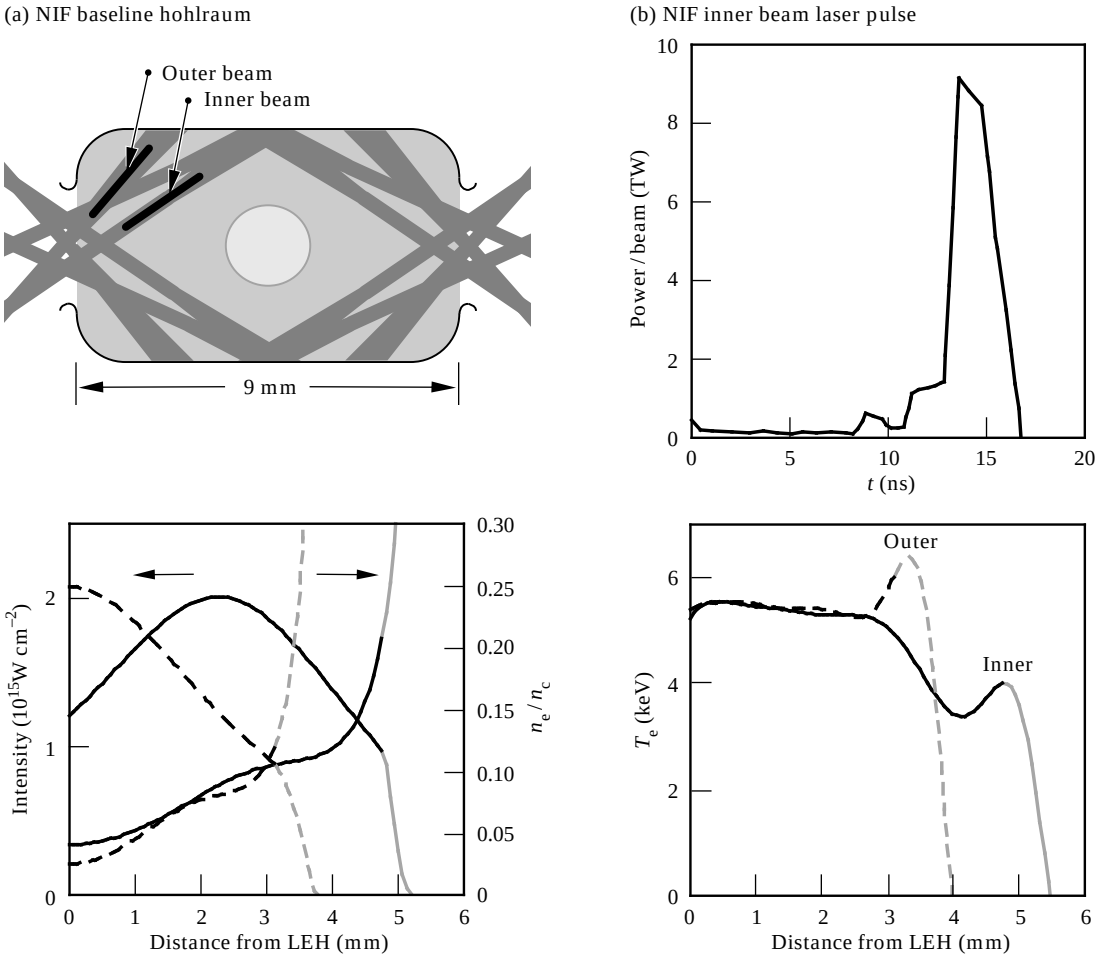

FIGURE 1. (a) NIF baseline hohlraum, showing inner and outer beam cones; (b) power history for one NIF beam; (c) electron density (as a fraction of critical density $n_c = 9 \times 10^{21}$ cm^{-3}) and laser beam intensity vs position in NIF hohlraum at time of peak laser power. Laser beam incident from left. Dashed and solid curves represent parameters for outer and inner beam cones, respectively. Lighter portions of each curve indicate where the laser is interacting with Au plasma; other regions correspond to low-Z (a He/H mix) fill gas plasma. (d) Electron temperature for inner and outer beams. (20-07-1095-2434pb01)

The output from the 2-D hydrodynamics simulations of the NIF target can be post-processed with the Laser Interactions Post-processor (LIP)[6] to obtain the total gain exponent for SBS and SRS as a function of time and scattered-light wavelength. The calculated peak gain exponents along the path of a 2×10^{15} W cm^{-2} NIF beam are 25 for SRS and 30 for SBS. Figure 2 shows the post-processed linear gain exponents for SBS and SRS, as functions of scattered-light wavelength and of time throughout the NIF pulse, for the inner and outer beam cones. The plots show gray-scale contours of equal calculated gain exponent; darker regions correspond to higher gain exponent.

Figures 2(a) and (b) show the history of the SBS for the inner and outer beams, respectively. Some of the spectral features of the SBS gain calculations and differences between the inner-beam and outer-beam cases can be understood in terms of the plasma conditions under which the scattering would occur. For instance, Fig. 1(c) indicates that the inner beams traverse a longer length of low-density fill plasma than the outer beams. The SBS gain peaks at a wavelength of $\Delta\lambda \approx 14$ Å for the inner-beam case; for the outer beam, which has less path length in the low-Z plasma, the main spectral feature is a narrow gain spike at $\Delta\lambda \approx 7$ Å.

To understand these observations, consider that the wave-number-matching condition for SBS requires that

$$k_0 = k_s + k_{ia}, \quad (1)$$

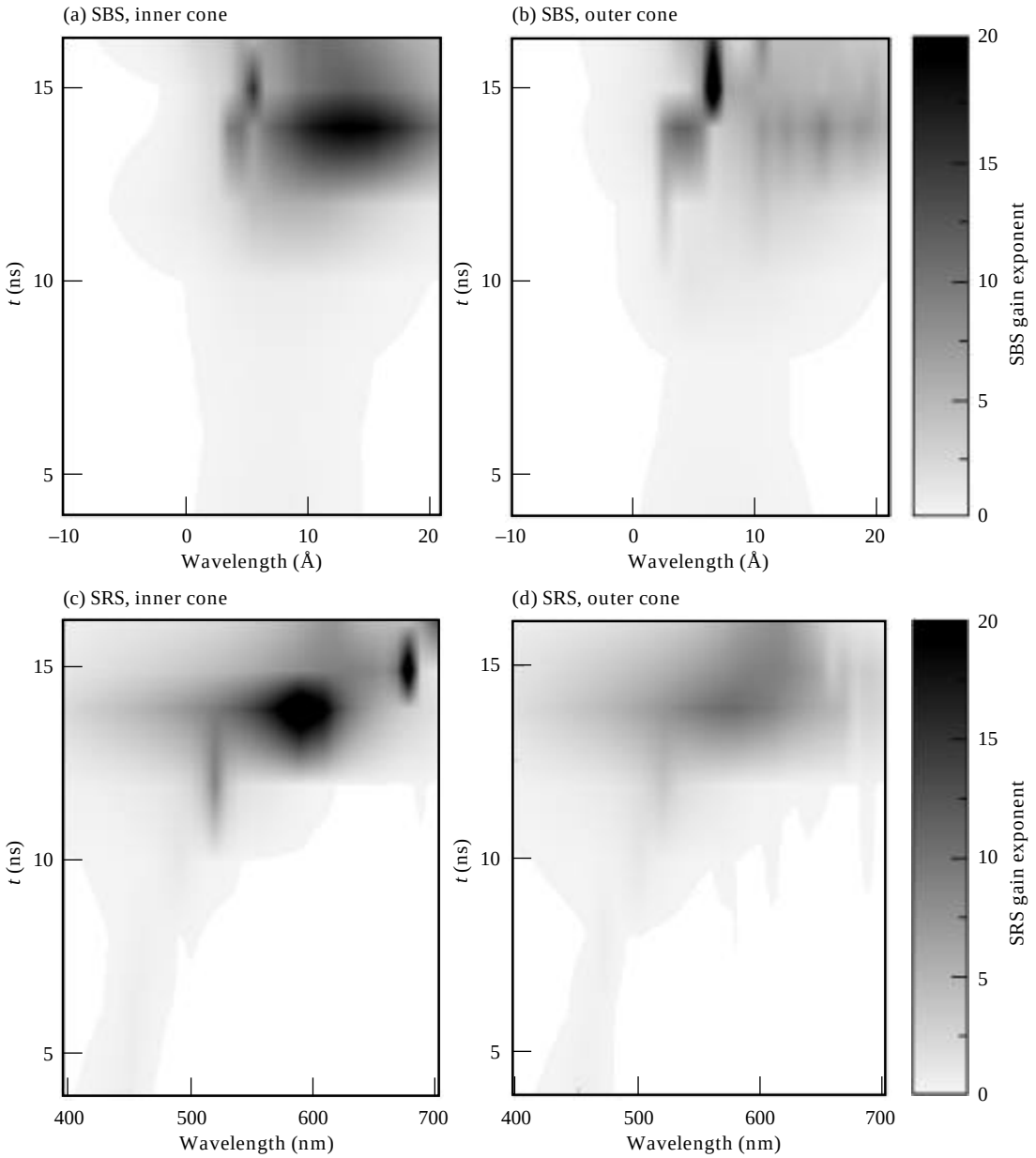

FIGURE 2. Post-processed (LIP) gain exponents along laser beam paths using plasma parameters from 2-D LASNEX hydrodynamics calculations of NIF. (a) SBS for inner cone; (b) SBS for outer cone; (c) SRS for inner cone; (d) SRS for outer cone. (20-07-1095-2435pb01)

where k_0 and k_s are the incident and scattered light wave vectors in the plasma. The wave number of the ion-acoustic wave k_{ia} has a magnitude equal to $2k_0$ for direct backscattering (since $k_s \approx -k_0$), where k_0 is related to the vacuum wave number k_{vac} of the light by

$$k_0 = k_{vac}\left(1 - n_e / n_c\right)^{1/2}; \quad (2)$$

this is a minor correction for densities near $0.1n_c$.

Although most of the incident photon energy goes into the backscattered photon, the ion-acoustic wave takes away some energy according to

$$\omega_0 = \omega_s + \omega_{ia}; \quad (3)$$

the frequency shift $\Delta\omega$ in the scattered light wave is therefore approximately

$$\Delta\omega = \omega_{ia} \approx 2k_0 c_s, \quad (4)$$

resulting in a wavelength shift

$$\Delta\lambda \approx 2\lambda_{vac}\left(1 - n_e / n_c\right)^{1/2} c_s / c, \quad (5)$$

where c_s is the sound speed. For a plasma flowing towards the observer with Mach number $M = v/c_s$, we have

$$\Delta\lambda \approx 2\lambda_{vac}\left(1 - n_e / n_c\right)^{1/2}\left(1 - M\right)c_s / c. \quad (6)$$

The strongest dependence here is on the sound speed and Mach number of the plasma in which the scattering is occurring. The sound speeds in Au and He/H are very different, because the sound speed scales as $[(Z_{eff}T_e + 3T_i)/A]^{1/2}$ and Au is a heavy atom ($Z < A/2$) that is not completely ionized (i.e., $Z_{eff} < Z$) while the low-Z plasma is fully ionized and has $Z \geq A/2$. Typical sound speeds are 3 to 4×10^7 cm s^{-1} for Au and 6 to 7×10^7 cm s^{-1} for He/H for the temperatures expected in the NIF plasma. The shifts in wavelength for SBS backscattering from Au and He/H are then 7 and 14 Å, respectively, for stationary plasmas. Note that flows in the plasma will also shift the scattered light wavelength according to the $[1 - M]$ term.

The feature at 7 Å appearing at 15 ns for the outer-beam SBS calculation [Fig. 2(b)] corresponds to SBS gain in the Au, with a peak gain exponent of 30. The broad gain peak at 14 Å in the inner-beam case [Fig. 2(a)] represents gain in the low-Z plasma with a peak gain exponent of 20. Although there is a small amount of gain at 6 Å in the inner-beam case, the observation can be made that the main SBS threat is from the wall material in the outer-beam case and from the low-Z fill gas in the inner-beam case. Hence we can break down the SBS problem into a high-Z problem, which is best addressed in experiments with Au walls (e.g., hohlraums), and a large, low-Z plasma SBS problem, which can be addressed in gas-filled hohlraums or with open-geometry gas targets.

The SRS gain exponents calculated by LIP are shown in Fig. 2(c) and (d) for the inner and outer beams, respectively. Figure 1(c) indicates that when the beams reach the Au they are absorbed in a short distance (~300 to 500 μm) in a region with steep density gradients. Since SRS gain is higher in large, homogeneous regions with shallow density gradients, most of the calculated SRS gain is in the low-density, low-Z plasma. Beams in the inner cone have higher expected SRS gain [with a maximum of 26, shown in Fig. 2(c)], because the beams have longer paths in the low-Z plasma, and the total exponentiation is a product of the spatial gain rate with the length over which that exponentiation can occur. The outer beams traverse less low-Z fill plasma and so have a lower calculated gain exponent for SRS [with a maximum of 11, shown in Fig. 2(d)].

The SRS plots show the calculated gain exponent for SRS as a function of the wavelength of the scattered photon. The wavelength of the scattered optical light carries information about the density and temperature of the plasma from which it scattered, because the electron plasma wave from which it scatters must satisfy

$$\omega_p^2 = \omega_{pe}^2 + v_T^2 k_p^2, \quad (7)$$

where ω_p and k_p are the frequency and wave number of the electron plasma wave, ω_{pe} is the plasma frequency (which introduces density dependence), and v_T is the electron thermal velocity (which introduces temperature dependence). The incident and scattered wave numbers are related by energy and momentum conservation:

$$\omega_0 = \omega_s + \omega_p, \quad (8)$$

$$k_0 = k_s + k_p, \quad (9)$$

where k_0 (ω_0) and k_s (ω_s) are the incident and scattered light wave vectors (frequencies). The wavelength of the scattered light that satisfies these conditions is strongly dependent on density and less strongly dependent on electron temperature. The large gain exponent at 590 nm for the inner beam corresponds to SRS growing at $n_e \approx 0.1n_c$ and a T_e = 3 to 4 keV. The long-scalelength targets described below were designed to explore this gain region. The lower-gain parts of the plot correspond to different densities within the NIF plasma; longer wavelengths correspond to higher densities. The small region of gain near 690 nm for the inner beam represents light scattering from plasma at $n_e \approx 0.2n_c$ and T_e = 4 keV. This region of plasma is low-Z material that has ablated from the capsule and produces

a slightly higher-density region of low-Z plasma where it collides with the Au wall. This region is difficult to reproduce experimentally and is less significant to the NIF problem because the laser energy in the part of the beam that reaches this plasma is very low because the laser light is being rapidly absorbed by this higher-density plasma.

As can be seen in Fig. 2, calculated gain exponents occasionally reach or exceed 20. Amplification of thermal fluctuations by 20 e-foldings is sufficient to produce both significant backscattering and plasma waves of sufficient amplitude that nonlinear saturation mechanisms begin to be important. The LIP calculations include no nonlinear effects, so the LIP results should be interpreted as telling us that there might be a significant scattering due to SBS and SRS in the NIF plasma for the period during which gain exponents exceed 20, but that we cannot predict the saturation level of that scattering. Hence we were motivated to try to reproduce plasma conditions with such gain exponents on Nova (where LIP can be used to compare the gains to the NIF case) in order to include saturation and other plasma effects that are omitted by the simple linear gain analysis.

The NIF beams will interact with the plasma at intensities up to 2×10^{15} W cm^{-2}, with a variation of intensity along the beam path as shown in Fig. 1(c). In the transverse direction, the laser intensity is assumed to be averaged over the beam profile, and the LIP calculations use this spatially averaged intensity. However, each beam is composed of small (~6 μm diam) speckles with a distribution of intensities above and below the average. The speckles can self-focus as they interact with the plasma, increasing the intensity within individual "hot spots," although beam smoothing such as smoothing by spectral dispersion (SSD), which moves the speckle pattern around rapidly, can reduce filamentation. This nonlinearity in the laser–plasma interaction is also omitted from the LIP calculations, so a further requirement of understanding laser–plasma interactions in the NIF by means of Nova-scale experiments was to use a laser beam with the intensity, smoothing, and f/number appropriate to a NIF beam. These experiments would address the legitimate concern that some fraction of each NIF beam will drive saturated levels of SBS and SRS and be reflected from the NIF hohlraum with the loss of energy and other consequences described above. The goals of these experiments were expressed in the HLP5/6 part of the 1993 NAS Nova Technical Contract as follows:

- HLP5: Demonstrate acceptable levels of scattering in large-scale plasmas that match the plasma conditions, beam geometry, and beam smoothing of ignition hohlraums as closely as possible. The plasmas should have density and velocity scalelengths ≈ 2 mm, electron temperature >1.5 keV, and $n_e / n_c < 0.15$.

Acceptable levels of scattering were defined as follows:

— Stimulated Brillouin scattering fraction f_{SBS} (back, side) < 5 to 10%.

— Stimulated Raman scattering fraction f_{SRS} (back, side) < 5 to 10% and f_{SRS} (forward) < 5%.

- HLP6: Evaluate the impact of laser beam filamentation on SBS and SRS and develop control techniques to the extent necessary to ensure acceptable levels of scattering.

Target/Plasma Development

To experimentally evaluate the severity of SRS and SBS scattering and filamentation on the propagation of an $f/8$ beam traversing a long-scalelength plasma, we reproduced the laser beam conditioning (f/number and smoothing) to be used on the NIF. At the same time, it was necessary to reproduce the plasma conditions expected within the NIF using plasmas produced by the Nova laser. Late 1993 and early 1994 saw a significant effort to produce plasmas that met the criteria expressed in the first part of the HLP5 statement of work. It was necessary to both reproduce the density (~$0.1n_c$) and temperature (at least 3 keV) of the NIF target but also to do so over a volume large enough that the total gain exponent of the NIF target for SBS and SRS could be approached.

Various targets were explored, including low-density foams and thin exploding foils. The most promising targets were large gas-filled hohlraums (of which two types were developed) and "gasbags." The plasmas were created by irradiating a thin-walled gas balloon or a sealed hohlraum[7] containing of order 1 atm of a low-Z gas (e.g., C_5H_{12}, C_5D_{12}, or CO_2). All three of these targets relied on heating a large volume of a heavy gas that, when ionized, produced the appropriate plasma conditions and was large enough to last for a reasonable time and to provide the right amount of SRS and SBS amplification.

Figure 3 shows the three targets developed to investigate laser–plasma interactions in NIF-scale plasmas. Figure 3(a) shows the GASBIG hohlraum, which is larger than the typical Nova hohlraum. Normal (scale-1) Nova hohlraums are the same length (~2.5 mm) but have a smaller diameter (1.6 mm), with the laser beams pointed so that they hit the wall before they reach the midplane of the hohlraum. The GASBIG hohlraums maximized the length over which the beams interacted with the plasma by pointing them at the opposite end of the hohlraum so that they crossed in the hohlraum mid plane. The hohlraum was filled with C_5H_{12} gas retained with a thin (6500 Å) polyimide window.

Figure 3(b) shows the toroidal hohlraum developed by LANL. This target produced a large length of plasma with which to interact by moving the wall of the standard Nova hohlraum radially outward to produce a more doughnut-shaped hohlraum. Figure 3(c) shows the open-geometry gasbag target, which was essentially two thin windows on either side of a thin washer. The target is inflated to make an almost spherical volume of gas. Figures 3(d) and (e) show density and temperature plots for the GASBIG and gasbag plasmas after they have been heated by the Nova laser beams, at the time at which the interaction with the NIF-like probe beam was studied (1 ns for the GASBIG, 750 ps for the gasbag). Both Figs. 3(d) and (e) show a relatively flat region of plasma near $0.1n_c$ at a temperature of 3 keV; this is the portion of the plasma that is approximating the region of high gain for SBS and SRS in the NIF inner beam.

The concept of producing a large, hot plasma by irradiating a gas-filled target has been discussed by Denavit and Phillion.[8] A cold gas volume of a few millimeters dimension can be heated by pulsed laser beams (typical duration 1 ns, intensity of order 10^{14} W cm^{-2}). When the laser beams strike the cold gas, a plasma is formed by multiphoton ionization. The initial low temperature of the plasma leads to energy deposition through inverse bremsstrahlung at the edge of the plasma. As that plasma is heated and becomes more transmissive, the laser beams propagate further into the gas. Our targets contained a high-molecular-weight gas (typically C_5H_{12}) that on ionization produced a plasma (electron) density $n_e = 10^{21}$ cm^{-3}. The velocity of propagation of the laser light into such a gas was measured for various laser conditions and is typically a few millimeters per nanosecond for 3ω light. For a 2.75-mm-diam gasbag plasma, the laser beams propagate to the center of the plasma by about 400 ps. Thereafter the laser beams steadily heat the plasma that they traverse; thermal conduction heats parts of the gas not directly irradiated by the laser beams. For the gasbag targets, the edge of the plasma is free to expand into the surrounding vacuum, so an isothermal rarefaction wave propagates towards the middle of the plasma at the ion sound speed (~0.5 mm / ns). The density plateau in the center of the plasma is therefore eroded by the converging rarefaction wave at a rate of about 1 mm / ns. After the plasma is formed and heated, we have a few hundred picoseconds to perform laser–plasma interaction experiments on our 2-mm size plasma before the rarefaction wave shrinks the

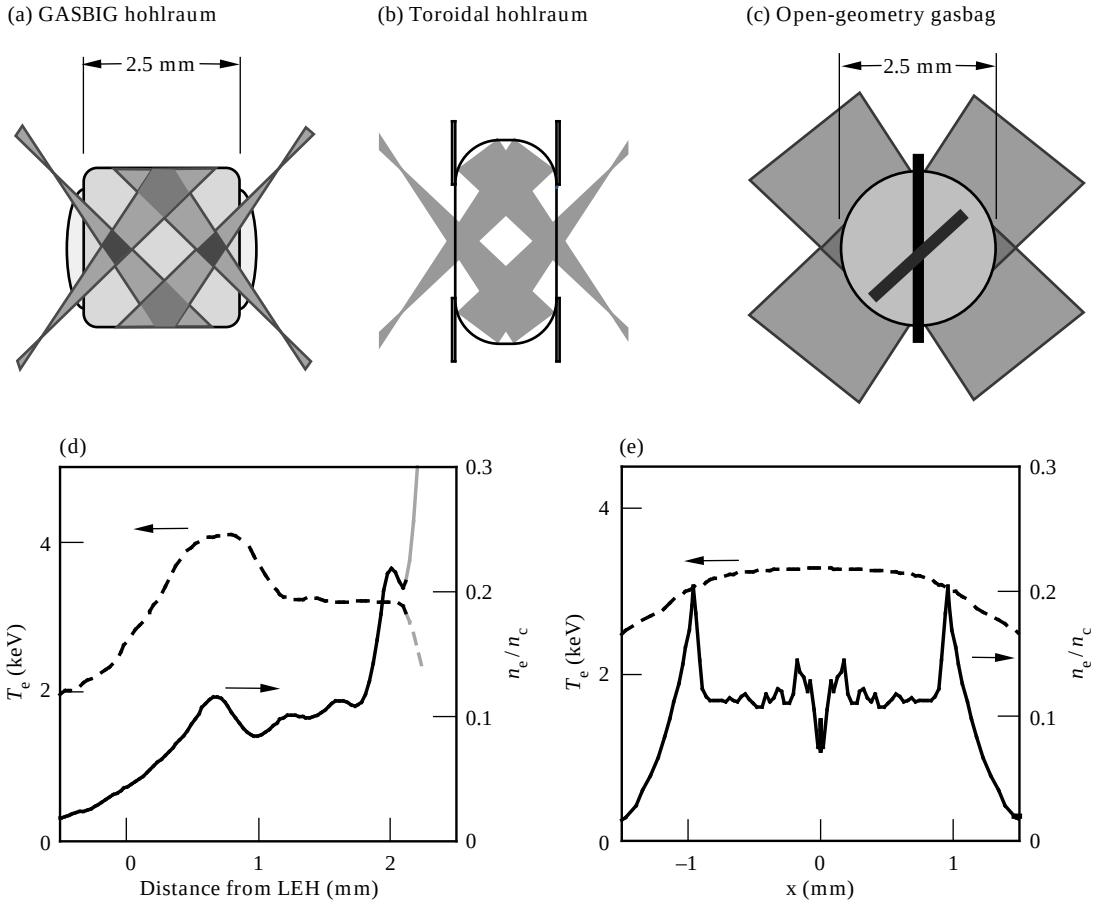

FIGURE 3. Targets developed to study laser–plasma interactions in long-scalelength plasmas similar to those of NIF. (a) GASBIG hohlraum; (b) toroidal hohlraum; (c) open-geometry gasbag target; (d) density and temperature for GASBIG hohlraum targets at a time (1 ns) at which interaction with NIF-like probe beam was studied. Lighter part of each curve indicates Au plasma. (e) Density and temperature for gasbag target at a time (750 ps) at which interaction with NIF-like probe beam was studied. (20-07-1095-2436pb01)

density plateau and so reduces the length available for amplification of SBS and SRS.

For each of the three targets, there was a period during which the plasma was ionized and heated using nine of the Nova beams. For the gasbags these "heater" beams were on for 1 ns; the interaction beam was turned on at t = 500 ps and also lasted for 1 ns. There is therefore a 500-ps period during which the heaters and interaction beams overlap in time. During this period the plasma temperature is still rising. When the heater beams turn off there is a 500-ps period during which the plasma is cooling but the interaction beam remains on.

The balloon targets were constructed by placing a thin membrane of polyimide ($C_{14}H_6O_4N_2$) on each side of a thin (400 μm) washer. The membranes were then inflated to an almost hemispherical shape through hypodermic fill tubes that penetrated the washer. Figure 3(c) shows the target and the laser-beam focusing geometry used to heat the plasma. Nine heater beams with a total energy of 18 to 22 kJ in a 1-ns pulse were used to create the plasma.

Unlike the more traditional targets for high-density laser–plasma interactions (solid or exploding-foil targets) the gas balloon targets convert most of the incident heater laser energy into thermal energy of the electrons and less into kinetic energy of bulk plasma motion. The energy budget for a typical gas balloon simulation is 22 kJ incident, 12.5 kJ absorbed, 8.8 kJ in electron thermal energy (T_e = 3.2 keV) and only 2.6 kJ (21% of absorbed energy) in kinetic energy. These numbers should be compared with those for typical exploding-foil plasmas, for which similar calculations (to produce a $0.1n_c$ plasma) show 22 kJ incident, 8 kJ absorbed, 3.1 kJ in electron thermal energy (T_e = 2.4 keV) and 4.5 kJ in kinetic energy (56% of absorbed energy). The heating of a stationary low-density target is therefore a much more efficient way of producing a high-temperature plasma, and it has the added benefit that density and velocity gradients are much less severe and therefore more suitable for interaction experiments that mimic laser–plasma interactions within indirect-drive ICF hohlraums. Exploding-foil targets are excellent for producing the kind of flowing plasmas found in the corona around direct-drive ICF pellets.

Figure 4(a) shows a gated x-ray pinhole image of the plasma. The image is one of a series of gated images,

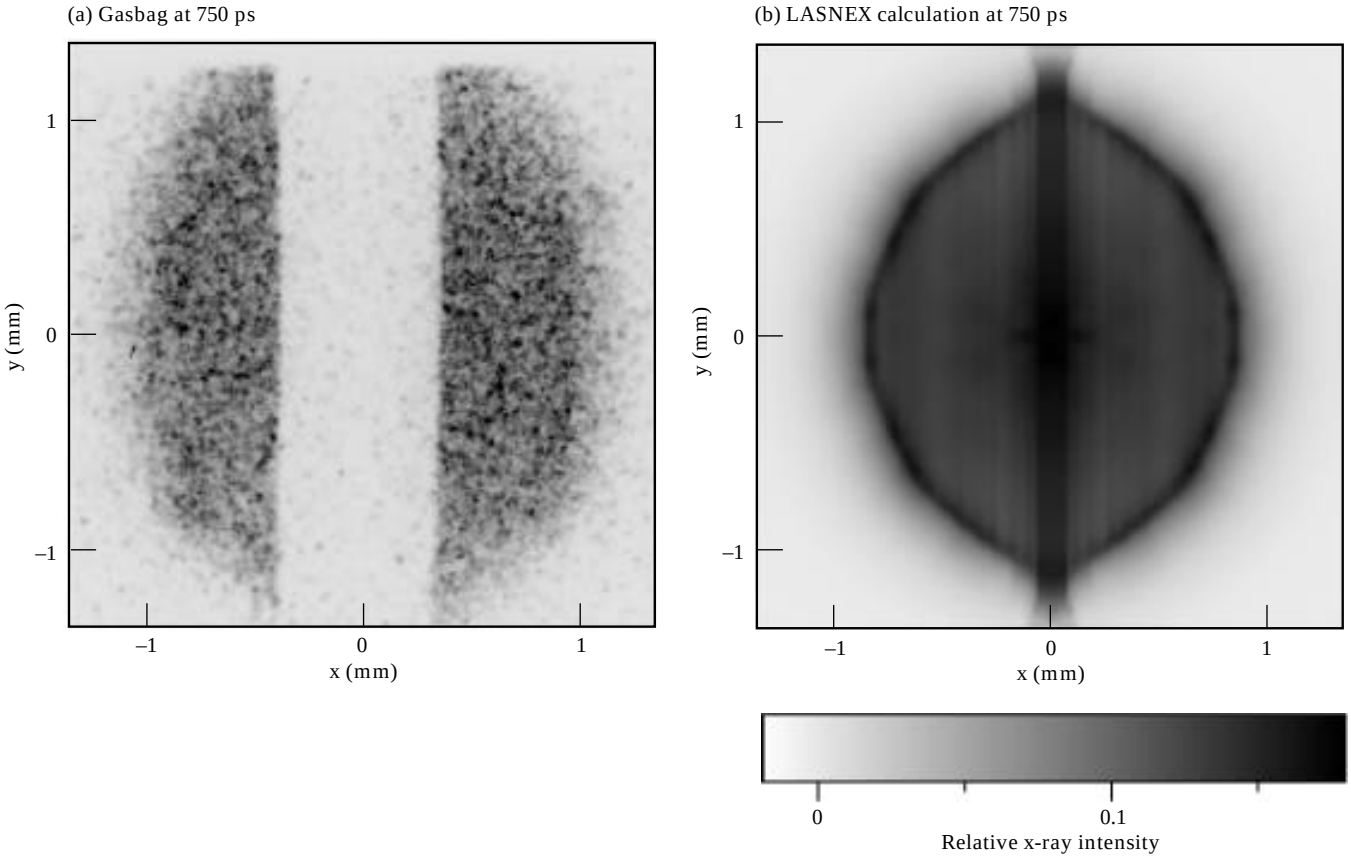

FIGURE 4. (a) Gated x-ray pinhole image of gasbag at 750 ps; large stripe across image is the shadow of a shield that is well away from the plane of the plasma. Support washer (shown in Fig 3c) is only 400 μm wide. (b) Simulated x-ray image from a LASNEX calculation at 750 ps. In both images, the gray scale indicates x-ray intensity integrated along the pinhole camera line of sight. Note the bright edge in this simulated image that is not seen in the data (a). The bright vertical stripe in the middle of the simulated image corresponds to a density peak that is propagating radially inwards in the plane of the washer. (20-07-1095-2437pb02)

with 100 ps time resolution, and was recorded 750 ps after the start of the heater pulses. The large vertical stripe across the image is not the support washer (shown in Fig. 3c) which is only 400 μm wide, but is the shadow of a shield that is well away from the plane of the plasma. The x-ray emission looks uniform within the limits of the microchannel plate noise; the camera was filtered to view x rays at photon energies above 1.5 keV, where the target was optically thin. The image represents the integration of x-ray emissivity along a chord through the plasma and could average changes in the emissivity caused by density fluctuations. Abel inversion of images such as this can show us if the plasma has a cold (less emissive) center, as is the case before the heater beams propagate to the center of the target. Some kind of 3-D tomographic imaging would be preferable, and we might eventually develop such a capability. Another alternative for better quantifying the uniformity of our plasmas is to do space-resolved thermal Thomson scattering using a 4ω (264 nm) probe beam. Again, this capability may be developed for future experiments.

The membrane that represents the initial bag wall perturbs the situation somewhat. The membrane is ~2000 to 3000 Å thick after the bag has been inflated and the material has stretched. The lasers heat the membrane, causing it to expand and rarefy, much like an exploding foil.[9] That process launches a weak shock into the bag, which propagates into the center of the target at about the sound speed. The peak density in this shock is calculated to be 2×10^{21} cm^{-3} for a C_5H_{12} gas fill [Fig. 3(e)]; the density scales with the fill density of the gas. Figure 4(b) shows a simulated image taken from a post-processed LASNEX calculation. A brightening due to this density peak is visible at the edge of the plasma. Although such a feature is seen at early times in our experiments, we do not see such a feature after the plasma has achieved its full size (at ~500 ps). The area in front of the shock wave is the region that has a flat density profile with no significant velocity gradients. The structure visible near the middle of the profile in Fig. 3(e) is produced by the symmetry of the calculation and has not been observed in experiments (with framing cameras viewing down the washer axis). The bright vertical stripe in the middle of the simulated image corresponds to a density peak that is propagating radially inwards in the plane of the washer. This peak has been seen in axial images, but it is never in the path of the interaction beam, which enters the plasma shown in Fig. 4(b) from 50° below the horizontal, crossing the image almost diagonally.

Electron temperatures were measured[10,11] by x-ray spectroscopy using K-shell line spectra from mid-*Z* elements (such as 2000 Å of cosputtered Ti and Cr or 2500 Å of KCl) placed in different locations inside the gas-filled targets. Analysis of the line intensity ratios uses a time-dependent collisional-radiative model of the plasma.[12] Isoelectronic ratios of the He-like emission were used because they are less affected by time-dependent ionization effects. Density variations are not expected to introduce large effects in the analysis and are included in the error estimates of the results.

The electron temperature in the C_5H_{12}-filled gasbag was measured with TiCr dopants and with Ar / Cl gas dopants. These spectroscopic measurements, using three different line ratios, consistently indicate that peak temperatures of 2.8 to 3.2 keV are achieved in the gasbags. Recent measurements of Ar and Cl satellite and resonance lines over several shots have enabled us to obtain a history of the temperature rise; these measurements show a peak temperature of 2.8 ± 0.5 keV, slightly below the LASNEX predictions. The measured temperature lags behind the temperature rise indicated by the simulation. Gasbags attain their peak electron temperature at 1 ns, when the heater beams turn off, but they are homogeneous after 400 ps when they are heated with 3ω heater beams.

The quoted electron temperature was measured in the gasbag plasmas with 3ω heater beams. Early experiments using 2ω (527 nm) heater beams (which would give higher temperatures because of increased collisional absorption) showed poor coupling of the laser energy into the initially cold plasma, which then stayed cold. Since $n_e = 10^{21}$ cm^{-3} is $0.25n_c$ for 2ω light, it was suspected that $2\omega_{pe}$ decay and / or SRS at the quarter-critical density was converting much of the incident energy to fast electrons,[13,14] which then deposited their energy in the target superstructure without heating the plasma effectively. Hence most of the experiments described here used 3ω heater beams and a 3ω interaction beam.

The electron temperature of the large gas-filled hohlraums ("GASBIGS") was determined using dopants deposited on 150-μm-wide, 800-Å-thick CH substrates. The gas volume of the hohlraums is not uniformly heated by the laser beams as in the gasbags, so the measurements were performed in and out of the beam path. Peak electron temperatures in the beam path of 3.6 keV were measured by the isoelectronic line intensity ratios of the He-like emission. Figure 5 shows the temperature history calculated by LASNEX and the corresponding measured temperatures. Measurements earlier than 1 ns are not included because accounting for the transient effects of the ablation and equilibration of the foil with the surrounding plasma introduces large uncertainties in the measurements. The temperature in the GASBIG is also observed to lag at early times. This discrepancy may be related to the heat capacity of the gas, because volumes not heated by the laser light must be heated by lateral heat flow; alternatively, it may imply that beam propagation is not as fast as the LASNEX calculation predicts. The out-of-beam measurements (not shown) show a temporal lag, but still achieve peak temperatures of 3 keV. Similar measurements using Ti / Cr spectroscopy made to characterize the toroidal hohlraum

plasmas[15] yielded temperatures of 3 ± 0.5 keV for the time at which the interaction beam would probe the plasma.

For all three of the targets shown in Fig. 3, we found temperatures of about 3 keV for plasmas of order 2 mm in size at $0.1n_c$. Since this approximates the region of the NIF plasma producing the highest calculated gain for SBS and SRS on the inner beam, we then turned to using these targets to perform interaction experiments. Note that the problem of producing a target with a gain similar to that seen on the outer beam in the Au [Fig. 2(b)] is not solved with these targets. None of them has sufficient radiation temperature to drive off a significant plateau of low-density Au plasma to mimic that region for the NIF outer beam. In fact, the scale-1 Nova hohlraums, when gas-filled, actually produce SBS gain exponents in the Au similar to that in the NIF outer beam. This occurs because inverse bremsstrahlung absorption in the Au, and not the hohlraum size, determines the scalelength in the Au. For gas-filled Nova scale-1 and NIF hohlraums, this absorption length is a few hundred micrometers. This issue is discussed towards the end of this article.

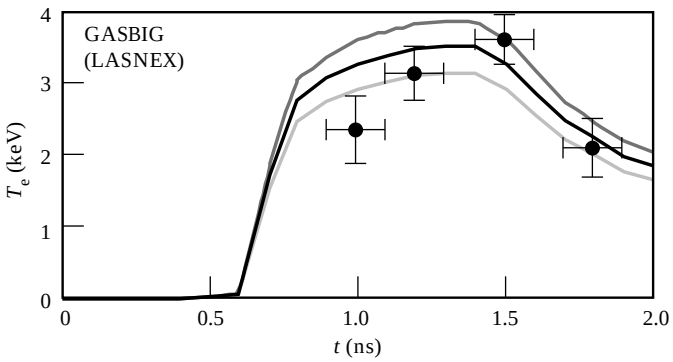

FIGURE 5. GASBIG hohlraum electron temperature history calculated by LASNEX, and corresponding measured temperatures. Top and bottom curves represent ±10% temperature variation.
(20-07-1095-2438pb01)

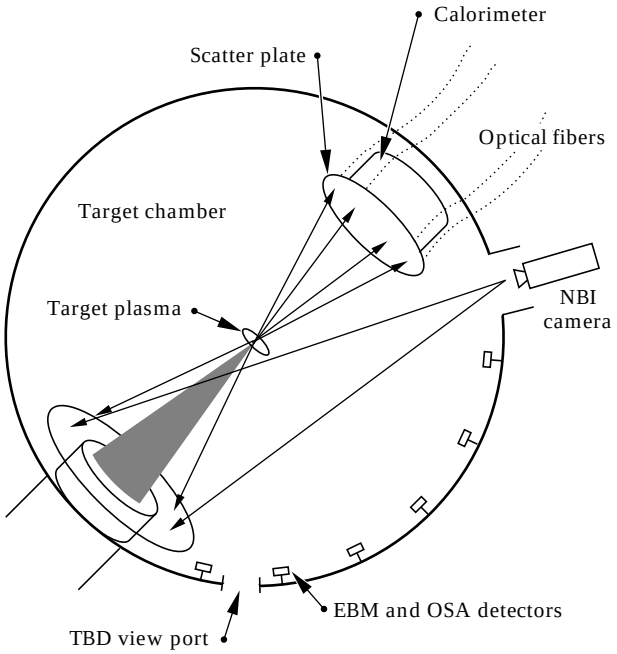

FIGURE 6. Nova target chamber, showing placement of scattered-light diagnostics. Beam shown is the interaction beam (beamline 7), on which the NIF beam smoothing and f/number were replicated. The other nine beams (used to heat the plasma) are not shown.
(20-07-1095-2439pb01)

Diagnostic Development

The development of diagnostics for the long-scale-length plasma experiments was motivated by the desire to better account for the scattered light and at the same time to quantify the light transmitted by the plasma. Figure 6 shows the placement of the various diagnostics in the Nova target chamber. The beam shown is the interaction beam (beamline 7), on which the NIF beam smoothing and f/number were replicated. The other nine beams (used to heat the plasma) are not shown.

Before 1993, measurements of SBS were made by taking a subaperture sample using a Fresnel reflector (uncoated beam splitter) within one of the ten Nova beams, and it was assumed that the backscatter was uniform within the beam aperture. The gain for both SBS and SRS peaks in the direct backscatter direction, so the scattered light should be collinear with the incident beam. In setting up for the long-scalelength plasma experiments, it was decided to move this diagnostic capability to the beam that we would use to mimic the NIF smoothing and focusing geometry, while making the system integrate backscatter over the full beam aperture. Figure 7 shows the new system, called the FABS (full-aperture backscatter diagnostic). The FABS views the scattered light that propagates back down the beamline and is transmitted by the 1ω (1054 nm) turning mirror closest to the chamber [which of course has high reflectivity (~95%) for the incident 1ω light but transmits ~30% of backscattered 3ω light]. A large hole was cut in the back of the mirror mounting box, allowing access to the scattered light transmitted by the mirror. Since light scattered from the target passes back through the Nova focusing lens, it is recollimated and is 70 cm in diameter when it emerges from the back of the mirror box. A second f/4.3 Nova lens was then used to focus the beam into the various diagnostic packages to allow analysis of the scattered light. A time-resolved SBS spectrometer, normalized with a time-integrating calorimeter, allowed the power history for SBS to be recorded; the time-resolved SBS spectrometer provided additional information on the spectral features of the SBS. A CCD camera also recorded a time-integrated image of the SBS backscatter angularly resolved within the diagnostic acceptance angle (i.e., SBS imaged in the plane of the Nova lens).

Viewing light scattered from the target through the Nova focus lens and refocusing it with a similar Nova lens introduces a large amount of chromatic aberration. The Nova lenses were intentionally designed with large chromatic aberration to separate the foci of 1ω, 2ω, and 3ω light (wavelengths 1054, 527, and 351 nm, respectively) in the target plane. This property causes problems when trying to focus the scattered light spectrum, which extends from 350 to 700 nm, into the diagnostic packages. A later version of the FABS will use a collecting mirror in place of the second lens and will correct the chromatic aberration through a series of small-aperture optics. This system[16] was not ready for the experiments described here; when it is implemented, it will have the capabilities of the current FABS but also will have the ability to image the target plane using the scattered light. The primary mission of the FABS in its original inception was to measure the SBS scattered light from the target. Because the SBS spectrum is quite narrow (~1 to 2 nm), the issue of chromatic aberration was not as severe as it is for broader-band SRS measurements.

SRS diagnosis was initially made through monitoring diodes placed 27° from the incident laser beam together with a streaked optical spectrometer. This setup was complemented by measurements of the fast-electron yield using the FFLEX filter–fluorescer, viewing x rays produced by electrons slowing down in the target material. As discussed below, the suspicion that SRS yields from targets were higher than implied by FFLEX led to the development of improved monitoring of the light scattered by SRS. The FABS diagnostic was modified (as indicated in Fig. 7) by having a diffuser placed soon after the focusing lens that scattered the light, which was then recorded by a filtered diode. This reduced the problem with chromatic aberration discussed above by making the measurement as close to the second focusing lens as possible, before the disparities in focal length could significantly change the beam size as a function of wavelength.

A further complication was introduced by severe modulations in the transmission of the turning mirror (inset in Fig. 7). The modulation is due to the multilayer coating on the mirror, which is optimized to reflect narrow-band 1ω laser light efficiently, not to transmit a broad-band signal. This modulation makes quantitative measurements of SRS difficult. The difficulty was addressed by using a streaked optical spectrometer to spectrally resolve the SRS signal seen by the diode. The spectrum could then be corrected using the calibrated mirror transmission function, and the diode signal (which represents an integral of the spectrum) could be corrected accordingly. This spectrometer also allowed us to record the spectrally resolved SRS reflectivity for comparison with our expectations [e.g., Figs. 2(c) and (d)] and also to study changes in the spectrum as a function of beam smoothing and laser *f*/number. All of the SRS spectra shown below were corrected to remove the modulation of the mirror transmission.

The FABS diagnostic was calibrated by using an uncoated spherical mirror placed on the far side of the chamber from the instrumented beamline (beamline 7). Beam 7 was then focused through a large hole (~6 mm diam) in a plate positioned at chamber center. The plate absorbed the unwanted harmonics of the laser beam (e.g., 1ω and 2ω in the case of a 3ω calibration shot), because the chromatic aberration in the Nova lens meant that only one color was focused at the hole. The light then diverged before it was reflected by the uncoated mirror and sent back down the beamline, where is was recorded as a known amount (~6%) of backscattered light.

The SBS detectors were calibrated using the 3ω calibration shots that are run routinely to maintain confidence in the precision Nova incident-beam diagnostics. To calibrate the SRS detectors, 2ω light was used, since its wavelength is in the middle of the spectral range of SRS light from most of our experiments. The sensitivity of the other components in the diagnostic relative to their sensitivity at 2ω were calibrated off-line. This process resulted in a typical uncertainty of 10% in the SBS and 20% in the FABS SRS measurements.

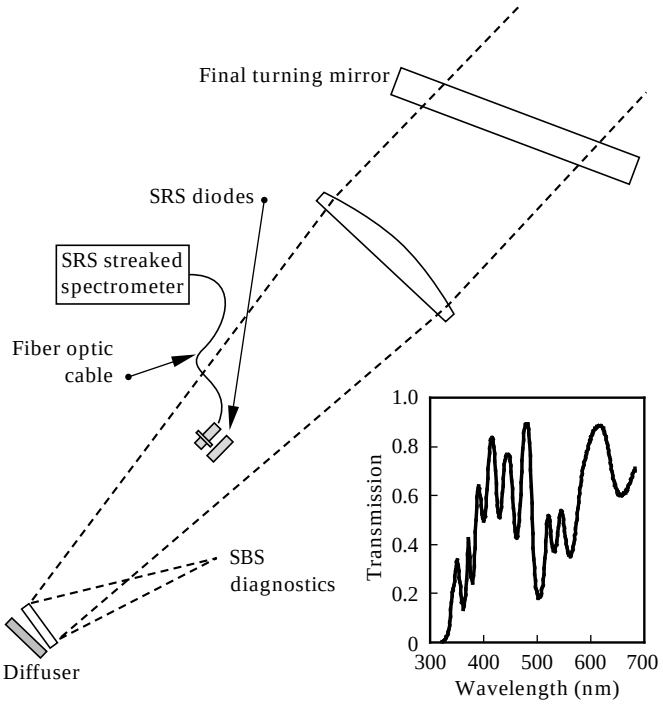

FIGURE 7. Full-aperture backscattering station (FABS) diagnostic, and (inset) transmission of final 1ω turning mirror through which FABS views scattered light. SBS light is reflected from a beam-splitter before it is injected into the SBS diagnostic package. A diffuser behind the beam-splitter reflects broader-band light into the SRS diagnostics. (20-07-1095-2440pb01)

To complement the FABS, the diagnostic set included time-integrated diodes (Fig. 6) spaced at ~10° intervals around the chamber to look at sidescattered light. As discussed below, there were indications in the first experiments with these diagnostics that the scattered SBS was coming back outside the collection angle of the FABS (defined by the incident beam *f*/number). Initial estimates were therefore made of the energy outside the lens using similar time-integrated diodes. An estimate of the spreading of the backscattered SBS was also obtained by restricting the aperture of the incident beam and using the FABS to image the light that scattered outside the angle of the incident sub-aperture beam. These estimates led us to conclude that up to three times as much scattered SBS energy may have been outside the lens as inside it for gasbag targets. At the time, the precision of this measurement was sufficient, because the amount of SBS in the lens was negligible. However, in the second phase of the experiments we planned to push the amount of SBS upward, so we expected that the energy outside the lens would play a large part in determining the energy budget of the interaction beam. Therefore a new diagnostic for near backscattered light was developed for the second series of experiments.

The near-backscattering imager (NBI) extended the continuous coverage of SBS and SRS backscattering outside the lens to 20° from the lens axis. This was achieved by placing a large annular plate of bead-blasted aluminum around the outside of the lens assembly within the target chamber (Fig. 6). The near-backscattered light from the target scatters from the plate as if from a diffuse screen and is then imaged by two TV cameras on the far side of the target chamber. Filters on the TV cameras allowed us to separately measure SBS (near 351 nm) and SRS (400 to 700 nm). Off-line calibration of the plate reflectivity and the known filter and TV camera throughput allowed us to spatially integrate an image frame at shot time to determine the total amount of scattered light. The images could also be combined with the images recorded by the FABS SBS and SRS cameras to provide an image of the angular distribution of scattering inside and outside the interaction beam solid angle. The diagnostic was supplemented by time-integrated diodes and fiber optics viewing the target through holes in the plate. The fiber optics allowed samples of the scattered light to be transported to an optical streak camera, where differences in time history as a function of scattering angle could be quantified.

The calibration of the plate reflectivity plus camera sensitivity could be checked *in situ* by comparing the scattered intensity with that recorded on the diodes. We could also compare the sensitivity of the FABS and the NBI by using a Au foil target at the chamber center to reflect energy from one of the other beam lines towards beam 7. This technique uses the "glint" reflected from the Au foil to fill both diagnostics with light. Comparison of the glint imaged in both diagnostics then revealed any inconsistencies as sharp jumps in image intensity where the coverage of the two diagnostics abutted one another. Contamination of the plate by target debris is a potential source of inconsistency. Initially a large effort was made to compare NBI and FABS to keep confidence in the calibration of NBI. As the use of the NBI diagnostic has become more routine, we have instituted a schedule of installation, removal, and recalibration of sections of the plate, and we use the diodes inset in the plate to maintain confidence in the evolution of the calibration. Problems with the time-integrating diodes (described below) have been eliminated by using more linear diodes with better dynamic range. The uncertainty in the NBI SRS and SBS numbers is about 30% for the data discussed below.

Sidescattered SBS light in these experiments was studied with a diode array. The diodes were time-integrating, so they could not distinguish the contributions due to sidescattering from the heater beams. The solution to this problem was to put fiber optics inside the chamber beside each diode to relay the SBS light from there to an optical streak camera, which then provided a time-resolved history of the sidescattering that could be normalized with the time-integrated diode signal. The contributions due to sidescattering from the heater beams could then be seen occurring early in time; those due to the interaction beam would come later. This system of combined diodes and fiber optics was called the oblique scattering array (OSA).[16] The system was not operational during the first *f*/8 campaign (April 1994) and was only partially operational during the second *f*/8 campaign (February 1995). In all applications involving diode measurements, it was necessary to absolutely calibrate the detectors, filters, and blast shields off-line and then monitor how their calibration changed in the target chamber due to debris buildup by frequent recalibration and replacement of debris shields and filters. During the first *f*/8 campaign, when the diodes were being used to quantify SBS near backscatter outside the lens cone, the diodes became nonlinear in their sensitivity to 3ω light at distressingly low fluences. This effect required characterization of the diode sensitivity over a wide range of incident fluences and also reduced the effective dynamic range of the diodes.[17] Individual diode readings fluctuated from shot to shot, and diodes next to one another often gave conflicting measurements. This may have been due to diode nonlinearity or damage or to small-scale structure in the scattered light intensity, which is difficult to resolve with single-point diode measurements. This latter consideration was one motivation for making the imaging NBI system for near backscatter. We may build a similar imaging system for sidescatter that will avoid the poor statistics of the single-point diode

measurements. New diodes were identified that had better dynamic range and that were linear up to higher fluences. These diodes were installed in the NBI plate as described above and were retrofitted into the OSA array.

The last diagnostic shown in Fig. 6 is the Transmitted Beam Diagnostic (TBD), whose purpose is to measure the amount of light transmitted by our open-geometry plasmas and to study the effect of processes such as diffraction from filaments on the divergence of the transmitted beam. This diagnostic was first set up during the 1994 $f/8$ campaign. The device was a frosted glass plate mounted on the opposite side of the chamber from Beam 7 (see Fig. 6). In its original form, the plate intercepted, transmitted, and forward-scattered light over an angle equivalent to $f/7.2$. However, it was quickly realized that the beam expanded beyond the $f/8$ original beam divergence as a consequence of refraction, diffraction in filaments, or forward SBS. For the second $f/8$ campaign, the TBD was enlarged to detect light over a $f/3.6$ cone. The plate was viewed by an optical framing camera that recorded the beam angular spread at four distinct times, together with a streak camera that resolved the divergence in one dimension continuously in time. Absolute measurement of the transmitted light was made using a fast diode that gave the history of the beam integrated in both spatial dimensions. The system was calibrated by firing a shot with known 3ω laser energy through an aperture placed at chamber center to remove the 1ω and 2ω light. A secondary measurement made with the TBD system was quantification of forward Raman scattering by injecting some of the transmitted light through a fiber optic into a low-resolution streaked optical spectrometer. Fiber-optic coupling was also used to inject the forward-scattered light into a high-resolution spectrometer to investigate the effects of filamentation on laser wavelength.

The main purpose of the TBD was to reveal changes in transmission due to the onset of scattering processes. Quantifying all the loss mechanisms due to parametric processes is very difficult. However, since the main objective of our experiments is to show that we can propagate a NIF-like beam through a NIF-like plasma without adverse effects, it was decided that by looking at the beam after it has traversed such a plasma we can directly discern if some as-yet unquantified process is serving as a loss mechanism. By looking at the characteristics of the beam after it has passed through one of our open-geometry gasbag plasmas, as a function of beam smoothing and laser intensity, we can ensure that the laser will propagate according to design in the NIF hohlraum.

1994 NIF Experiments

In April 1994 the NIF beam geometry was reproduced on Nova by modifying one beam to have the $f/$number and smoothing characteristics of a cluster of four NIF beamlets. Nine of the Nova beams were used to produce the long-scalelength plasma; the tenth was configured as an interaction beam that was sent through the preformed plasma after a 500-ps delay. The SRS and SBS scattered from the plasma, together with the effects of the plasma on the transmitted beam, were studied as a function of the interaction beam intensity, beam smoothing, and plasma constituents. The interaction beam was smoothed by using RPPs,[18] and four different colors within the $f/8$ beam to mimic the NIF laser architecture.[19] The four-color setup divided the $f/8$ beam into four separate quadrants, each of which had its wavelength shifted relative to the others. The wavelength separation of the colors was approximately 1.4 Å at 3ω. Since each beam quadrant could have its frequency conversion crystals individually tuned for its wavelength, the four-color scheme approximated "bandwidth" on the interaction beam without losing 3ω conversion efficiency. We also studied the use of additional laser bandwidth of approximately 1.6 Å at 1ω on each color, coupled with SSD,[20] to further reduce reflected SBS. These studies were performed with both $f/4.3$ and $f/8$ interaction beam focusing.

The main results of the 1994 $f/8$ campaign were the observation of low amounts of SBS, with indications of more SBS scattered around the lens (a factor 2 or 3 in gasbags), but not enough to be a significant loss mechanism. Figure 8 shows the total SBS backscatter as a function of laser beam intensity and beam smoothing for the gasbag targets. The data are separated into the three smoothing conditions that were studied: four-color as described above, "one color," in which the four quadrants were set to be the same color, and "one-color SSD," which had an additional bandwidth of 1.6 Å at 1ω put on the one-color setup. The data plotted is the peak SBS reflectivity in time (reflected power/incident power), not corrected to account for SBS light reflected outside the lens acceptance angle. Our estimates based on the use of diodes to measure the energy outside the lens indicate that these numbers should be increased by a factor of 2 to 3, making the maximum SBS seen in these experiments only ~6%.

Low levels of SBS were observed for irradiances up to 6×10^{15} W cm^{-2} (well above that planned for the NIF). There was little difference in the levels observed with one-color or four-color irradiation; however, the addition of SSD beam smoothing to the one-color case reduced the SBS to below 0.5%. The observation of these low

scattering levels did raise the interesting possibility that the highest intensity planned for the NIF was too conservative, and that a design with higher laser beam intensity and hence higher hohlraum radiation temperature might be viable. The benefit in higher capsule gain and relaxed surface roughness specifications for instability growth made experiments at higher intensity very attractive.

The low level of SBS backscatter and the scaling of the SBS with intensity are perplexing. The apparent observation that four-color beam smoothing produces more SBS backscatter than one-color smoothing at high intensity was contrary to our expectation that four-color smoothing should suppress filamentation at least as well as one-color smoothing, if not better. The observation that SBS is reduced with the addition of a small amount of bandwidth and SSD beam smoothing is more sensible.

During this 1994 campaign we made the first transmitted-beam measurements, but these were limited to collecting light over an $f/7.2$ aperture; the transmitted $f/8$ probe beam broadened to overfill the detector, making quantification of the transmitted fraction uncertain.

Quantification of SRS backscattering from the long-scalelength plasmas was limited to large-angle diode measurements and measurements of the hard x-ray spectrum produced by fast electrons striking the Au hohlraum wall. These measurements showed that at most 1% of the incident energy was converted to fast electrons, with the limitation that the time-integrated technique did not distinguish between electrons produced by the heater beams and those produced by the probe beam. Experiments with the probe beam energy set to zero showed fast-electron yields similar to those with high power on the probe. In all of the interaction experiments carried out at $f/4.3$ and $f/8$ during this period, the inferred levels of SRS were low (<1%). This was perplexing, because a few experiments with gas-bag targets in the Two Beam chamber area of Nova produced larger levels of SRS (of the order of 4%). However, those experiments were done with plasmas that were cooler (1.5 keV) than the plasmas heated by nine Nova beams (3.2 keV). This observation is consistent with the higher temperature, in the plasmas heated with nine beams, resulting in strong electron Landau damping of the electron plasma waves at $0.1n_c$ for 3ω and so reducing SRS. In either case, however, the plasma should have had a peak gain exponent of at least 20 for SRS [e.g., Fig. 10(d), below]. The Two Beam experiments did not have a filter–fluorescer measurement for fast electrons produced by SRS. The SRS was measured by observing the scattered optical light that went back into the interaction beam lens. This difference motivated the installation of a similar optical SRS detection system in the Ten Beam chamber for the second $f/8$ campaign to better quantify SRS.

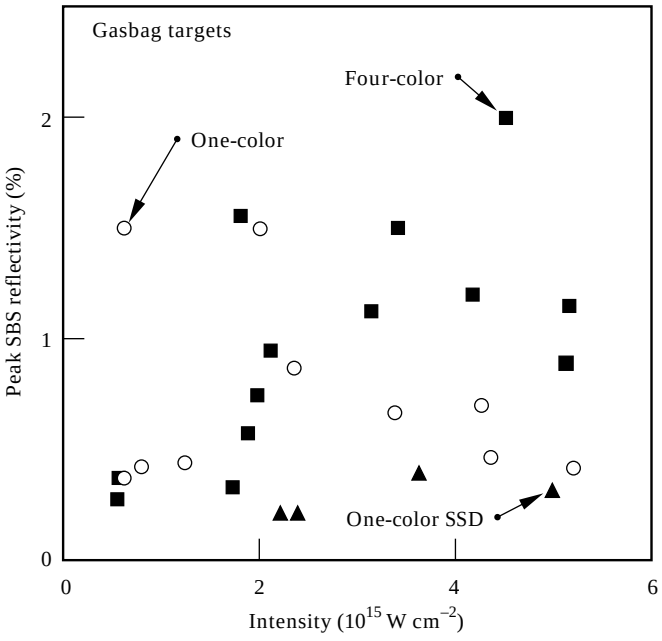

FIGURE 8. Measured SBS reflectivity from gasbag targets from April 1994 $f/8$ campaign. Quantity plotted is peak reflectivity (scattered power/incident power) into an $f/8$ collection angle; contributions due to scattering outside this solid angle are estimated to increase these numbers by a factor of 2 to 3. (20-07-1095-2441pb01)

Several issues were left unresolved by the first $f/8$ campaign:

1. The effectiveness of SSD beam smoothing in suppressing filamentation and how it compared with four-color smoothing.
2. The effectiveness of four-color versus one-color beam smoothing in suppressing filamentation.
3. The low level of SBS.
4. The low level of SRS inferred from FFLEX.
5. No real quantification of the characteristics of the transmitted beam.
6. Sidescattering was not quantified.

Furthermore, the possibility of beams with different colors (e.g., four-color) transferring energy when crossing within the plasma had been raised by experiments that showed such an effect in long-wavelength (10.6 μm), low-density experiments.[21] This possibility merited investigation in more NIF-relevant plasmas using 3ω light.

For the initial $f/8$ experiments, the peak SBS observed from the C_5H_{12} plasmas was less than 6% for all irradiation conditions tested. It was therefore decided to perform a second series of $f/8$ experiments

with improved diagnostic capability to explore higher intensities than those expected in the NIF baseline design. These experiments would also attempt to resolve the issue of what beam smoothing is most effective for the NIF; however, these initial results were encouraging.

Ion-Landau Damping Experiments

To address the issue of low levels of SBS in our NIF-like plasmas, we looked at data obtained from plasmas that had a reduced level of ion-Landau damping. Some experiments carried out at $f/4.3$ showed that changing the material in the target to one with a lower expected ion Landau damping of sound waves led to a strong increase in SBS. Figure 9 shows the results of an experiment performed at $f/4.3$ that investigated the effect of removing the light ions (protons) from the plasma. Since the hydrogen ions in C_5H_{12} are lighter than the carbon ions, their average velocity is significantly higher than that of carbon ions at the same ion temperature. The presence of these faster protons near the phase velocity of the ion-acoustic wave, which is pumped by the SBS process, allows them to extract energy from the wave and so damp it.

The data in Fig. 9(a) are from gasbag targets with a variety of gas fills. Backscattering levels as high as 35% were observed for CO_2 plasmas, while subtly changing

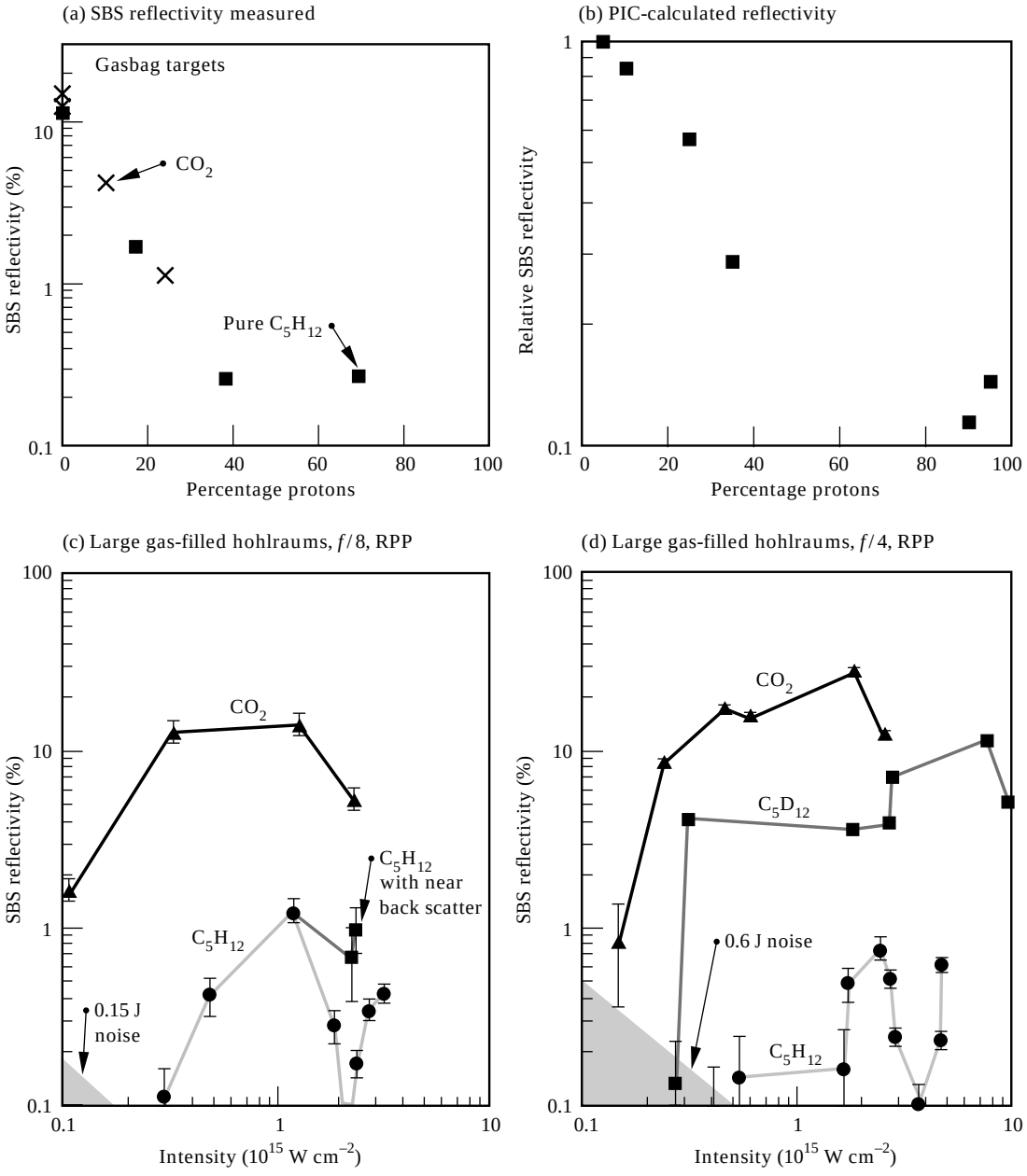

FIGURE 9. (a) Time-integrated SBS reflectivity from gasbag targets containing mixtures of CO_2 and C_3H_8 (crosses) or C_5D_{12} and C_5H_{12} (solid squares). The amount of the second material is varied and is expressed as percentage of ions that are protons vs proton concentration. (b) PIC calculation of SBS reflectivity from a CH plasma (normalized to unity for pure carbon) vs proton concentration. (c) Time integrated SBS backscatter from toroidal hohlraums, $f/8$ experiments; (d) SBS back-scatter from toroidal hohlraums, $f/4$ experiments. (20-07-1095-2442pb01)

the plasma from C_5H_{12} to C_5D_{12} (i.e., changing protons to deuterons) increased the peak SBS from ~3% to ~25%. Both CO_2 and C_5D_{12} are expected to have lower ion Landau damping than C_5H_{12} at the range of ion temperatures expected in the experiments.[22] The higher damping of the C_5H_{12} plasma arises because of the mixing of a light ion (H) that does the damping with a heavier ion (C) that determines the sound speed. The high thermal speed of the hydrogen relative to the ion-acoustic wave speed allows the many protons moving at the wave speed to efficiently extract energy from the wave, damping the wave and reducing the SBS gain. This phenomenon was first reported by Clayton[23] in low-T_e, low-density discharge plasmas irradiated with 10.6-μm CO_2 laser light. The experiment reported here was the first observation of this effect in a high-T_e, high-density plasma relevant to ICF. To demonstrate that the protons within the plasma provided the damping, Clayton altered the concentration of hydrogen in the plasma and observed the effect on the SBS threshold. We performed similar measurements with our C_5D_{12} and CO_2 plasmas by adding small concentrations of C_5H_{12} or C_3H_8 to provide more protons. The gasbag experiments did not attempt to measure an intensity threshold for SBS, but instead kept the average intensity in the target fixed and varied the proton concentration.

Figure 9(a) shows the results, which illustrate the reduction in total SBS with increasing proton density. The SBS that we see has essentially saturated. This result has been modeled and essentially reproduced with PIC simulations [see Fig. 9(b)],[24] which is interesting because the ion-Landau damping argument is an argument for a reduction in the linear gain for SBS. The PIC calculations obviously include this linear mechanism plus important nonlinear kinetics effects such as particle trapping and nonlinear frequency shifts. These latter effects reduce the gain beyond what would be calculated with the linear damping only. Figure 9(b) shows the calculated SBS reflectivity for a CH plasma, as a function of proton concentration, normalized to unity for pure carbon. The calculation gave a reflectivity of about 70% for this case. Note that a 1-D PIC simulation always overestimates the SBS reflectivity, because 2-D and 3-D effects that can also limit ion wave growth are obviously omitted.

Figures 9(c) and (d) show SBS reflectivity data (reflected energy / incident energy of the interaction beam) for the toroidal hohlraum experiments. These data are from the 1994 $f/8$ series and from subsequent experiments carried out at $f/4$. The figures also show the effect of the ion species on SBS reflectivity. The reflectivity appears to correlate inversely with the Landau damping rates of the SBS ion wave. For these hohlraum conditions ($T_i/T_e \approx 0.2$), the estimated Landau damping rates normalized to the ion-acoustic frequency (ν_i/ω_i) for He / H, C_5H_{12}, C_5D_{12}, He, and CO_2 are 0.35, 0.25, 0.15, 0.01, and 0.01, respectively.

The plasmas we have produced seem homogeneous enough that the SBS is sensitive to the damping from different materials. This effect was not observed in exploding-foil experiments,[25] in which the SBS reflectivities of CH and Ti plasmas were similar, presumably because of the large flow gradients ($L_v \approx 300$ μm), which reduce the effective interaction length because of dephasing proportional to the acoustic wave damping rate. The total gain is equal to the product of the gain rate ($\sim 1/\nu_a$) and the interaction length ($\sim \nu_a L_v/\omega_a$) and is then independent of the damping rate. Since our results show an SBS reflectivity that is sensitive to damping, they may indicate that the interaction length is being determined by something other than the velocity gradient scalelength L_v. We are continuing to study the relation between velocity gradients in our long-scalelength targets and those expected in NIF plasmas. Because our results show an SBS reflectivity that is sensitive to damping, they suggest that the interaction length is not dominated by inhomogeneities such as the global velocity-gradient scalelength L_v. Fluctuations in the velocity cannot be ruled out, but they should be similar in NIF plasmas to those in our long-scalelength targets, because the initial gases are uniform and nonuniformities are produced by similar laser heating processes.

The phenomenon of enhanced damping by adding protons to the plasma will be used in NIF hohlraums by filling them with mixtures of H_2 and He. Calculations indicate that this mixture will provide even higher ion-Landau damping than in our C_5H_{12} experiments.[22] The LIP calculations for the NIF plasma use the damping appropriate for this He / H mixture. The gain exponent of 20 for the inner beam SBS taking place in the low-Z plasma already takes into account the large ion-Landau damping in such a plasma.

1995 NIF Experiments

As discussed above, the first round of $f/8$ laser–plasma interaction experiments left many issues unresolved. After the diagnostic development described above, we embarked on a second $f/8$ campaign with the intent of finding the optimum smoothing required for the NIF and of determining the beam intensity above which laser–plasma instabilities prevented efficient beam propagation.

In this section we describe these most recent experiments and present some of the details of the experimental observations that were omitted in previous sections. Gasbag, GASBIG hohlraums, and toroidal hohlraum targets were all used in these experiments. The main results were that the levels of SRS backscattering were higher than inferred previously with the FFLEX

technique. The SRS was collimated so that it came back straight into the lens. The levels of SBS were even lower than those observed previously; in fact, there is the distinct possibility that those measurements were contaminated by SRS getting into the SBS calorimeter. The levels of backscattering were sensitive to beam smoothing in the form of SSD and insensitive to differences between four-color or one-color beam smoothing. Scattering at 2×10^{15} W cm^{-2} was at a level acceptable in NIF designs, but higher intensities produced far more SRS. The NBI diagnostic showed that the SBS scattered outside the lens multiplied the FABS-only number by a factor of 2 to 3 for gasbags, but GASBIG hohlraums produced much less symmetric SBS backscattering that had as much as a factor of 10 more SBS outside $f/8$ than inside it.

Figures 10(a) and (b) show gasbag SBS and SRS spectra recorded in the direct backscatter direction with the FABS diagnostic. The data are for a C_5H_{12}-filled gasbag irradiated with 2.2×10^{15} W cm^{-2} with a four-color $f/8$ beam with 1.6 Å of SSD beam smoothing. Figure 10(a) shows SBS spectra recorded from the gasbag plasma. Early in time (0 to 500 ps) the spectrum shows sidescattering from the nine heater beams scattering from the cold gasbag. The sidescattering contribution is small (~20 J/sr) and fades at later time (~500 ps) as the plasma heats up and the density peaks at the edge subside. Data taken with only heater beams (i.e., no interaction beam) show the same signals up to 500 ps. At 500 ps, the interaction beam turns on and produces a narrow SBS spectrum with a red shift of about 10 Å. This shift is consistent with that expected

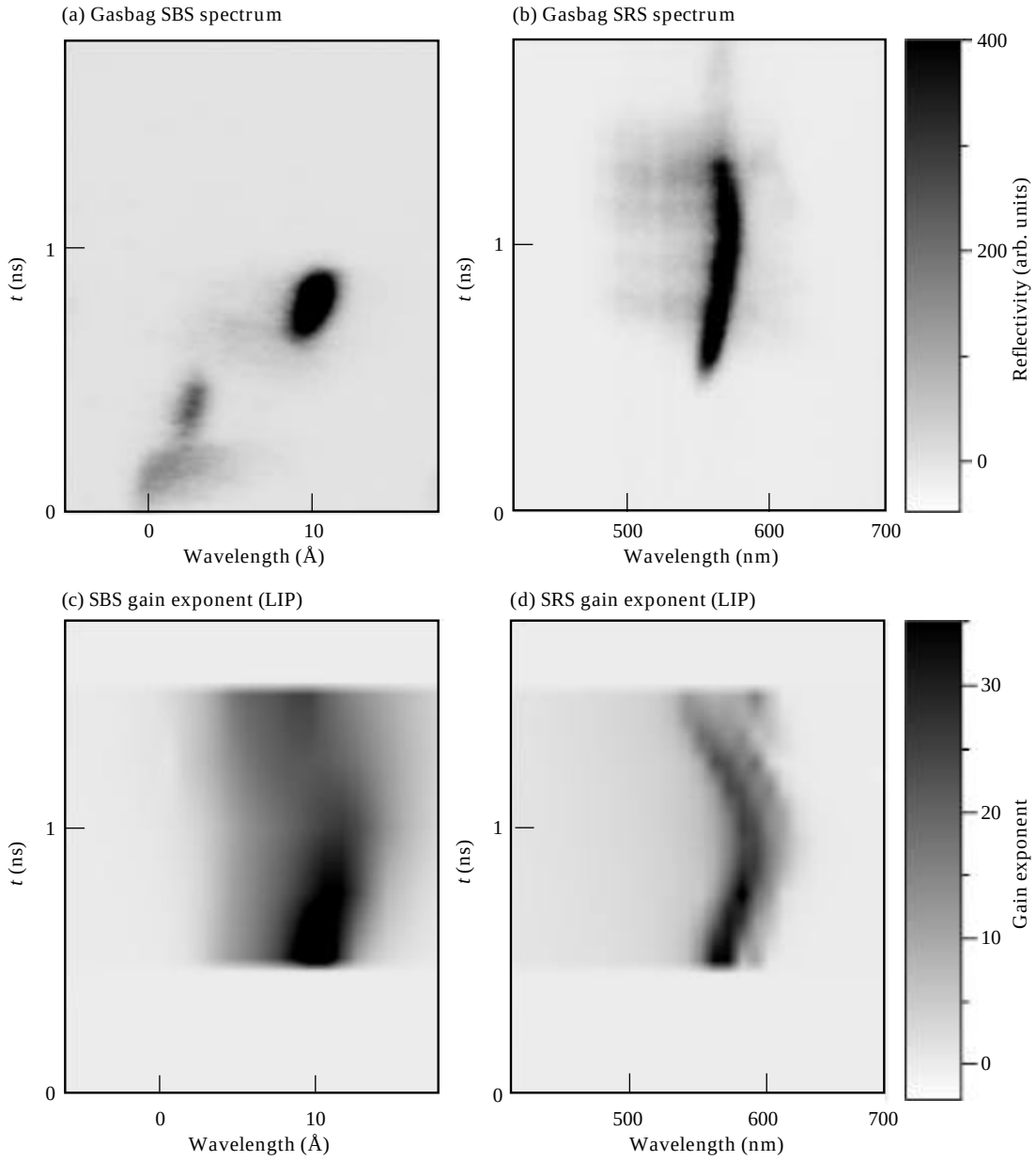

FIGURE 10. Gasbag SBS and SRS spectra. (a) Time-resolved SBS spectrum; features appearing up to 500 ps are sidescattering contributions from the nine heater beams interacting with a bag that is initially cold with high density at the edge. (b) Time-resolved SRS spectrum; (c) LIP-calculated gain exponent for SBS; (d) LIP-calculated gain exponent for SRS. (20-07-1095-2443pb01)

for SBS from a stationary C_5H_{12} plasma at 3 keV. This result can be compared with spectra from exploding-foil plasmas, for which the SBS spectrum is usually broad and blue-shifted, indicating that it may be coming from a plasma that is flowing, giving various amounts of Doppler shift to the backscattered light wave. The fact that there is no shift other than that expected from conservation of energy is a good indication that the plasma is stagnant and that velocity gradients are low. After 1 ns, the data show a strong reduction in the SBS signal.

The spectrum in Fig. 10(a) should be compared with the LIP gain exponent calculation using plasma parameters from a gasbag simulation, shown in Fig. 10(c). The calculation shows no gain before 500 ps, because the interaction beam is off LIP does not calculate sidescattering from the heater beams. After 500 ps, the calculation shows a narrow peak in the gain, which is 30 to 50 until 1 ns and then decreases. At late time, the gain exponent is reduced because the plasma is shrinking, making less interaction length available for amplification. The gain exponent is also decreasing because the ratio of ion to electron temperature is changing. The damping of SBS by ion-Landau damping is a strong function of this ratio (since the ion temperature determines the magnitude and slope of the ion distribution function at the ion wave speed, while the electron temperature determines the speed of the ion wave). At 1 ns, when the heater beams turn off, the electron temperature starts to fall and, since the ion temperature responds much more slowly, T_i / T_e rises rapidly, increasing the damping of SBS.

The correspondence between the gasbag SBS data and the LIP calculation is encouraging. The narrowness, red shift, and time history of the SBS spectrum are consistent, implying that we can predict the fundamental plasma parameters in the experiments. Since the gain exponent calculated at early time is 30 to 50, well in excess of that calculated in the NIF inner beam (20), the measured SBS reflectivity of ~0.2% for this experiment is promising for the NIF.

The LIP calculations [Fig. 10(d)] reproduce a number of features in the gasbag SRS spectrum shown in Fig. 10(b). The time history is interesting: there is a bright peak at 570 nm, which is consistent with SRS scattering from electron plasma waves in plasma at 9×10^{20} cm^{-3} (the average density of the plasma) and a temperature of 3.2 keV. The narrowness of the peak is consistent with a small range of densities that have sufficiently shallow density gradients to permit the growth of SRS. This narrow peak is reproduced in the LIP calculation shown in Fig. 10(d), but that calculation shows the peak at slightly longer wavelength (585 nm). Because the peak position depends on both temperature and density, it is possible that the disagreement arises because the plasma density or temperature is lower in the experiment than in the calculation. The peak moves towards long wavelengths from 500 ps to 1 ns, consistent with an increasing temperature, as the heater beams continue to deposit energy in the plasma. After 1 ns, when the heater beams turn off, the peak moves back to shorter wavelengths as the plasma cools. The peak movement associated with the rise and fall of the temperature is visible in the data, but the movement is not as great as in the simulation. The narrow SRS spectrum shown in Fig. 10(b) is reminiscent of those seen from exploding-foil plasmas, in which only the flat top of the density profile results in SRS because of the shallow density gradient there.[26]

Another remarkable feature in Fig. 10(b) is the scattered light that appears between 470 and 550 nm; this represents scattering from lower densities (0 to $0.1n_c$), which may be present as a result of filamentation. The short-wavelength SRS appears and disappears as a function of beam smoothing and intensity (as shown in Fig. 16, below). Both these parameters affect filamentation of hot spots in the beam. The short wavelengths also appear in Fig. 10(b) to increase as the plasma cools; again, this is consistent with a reduction of filamentation thresholds as the temperature is reduced. These observations are therefore consistent with the short-wavelength light coming from filaments where the high intensities produced by filamentation are needed to overcome the heavy electron-Landau damping of the electron plasma wave at such low densities.

For comparison, Figs. 11(a) and (b) show SBS and SRS spectra from C_5H_{12}-filled GASBIG hohlraum targets irradiated with 2.3×10^{15} W cm^{-2} with a four-color $f/8$ beam with 1.6 Å of SSD beam smoothing. The small amount of scattering seen at early time in Fig. 11(a) is light from the heater beams scattering from the thin membrane that constitutes the window of the hohlraum. The interaction beam is 1 ns long and turns on 1 ns after the heater beams; the heater beams have a long, shaped pulse that is on for the entire duration of the experiment. Once the SBS turns on, it is red-shifted as was the gasbag SBS, but it is not red-shifted as much and is broader than for the gasbag. Both these observations are consistent with a more ramped profile [such as that shown in Fig. 3(d)], which has plasma flowing towards the observer (back towards the laser entrance hole), giving a range of Doppler shifts to the SBS light. The SRS spectrum shown in Fig. 11(b) is also consistent with scattering from such a ramped profile. The lower wavelength SRS (500 to 550 nm) corresponds to densities below $0.1n_c$ (0.04 to $0.1n_c$). These lower densities may be on the profile or they may be present in filaments, as discussed above for the gasbag data. The time-integrated SBS and SRS reflectivities for this shot were 1.3 and 4.8%, respectively.

Figure 12 illustrates some of the combined FABS and NBI data showing the collimation of the SRS backscattering and the large blob of SBS from the hohlraum that

lies outside the FABS acceptance. The images are made by superposing the near-field image of the backscatter as seen by the FABS (0 to 3.6°) on the image recorded on the NBI camera (5.3 to 20°) to produce an image that covers 0 to 20° from the beam axis (a small annulus is missing between 3.6 and 5.3°). The SRS measurement is complicated by parallax in the view of the SRS camera inside the FABS, which results in distortion in the central part of the image. The examples shown in Fig. 12 are (a) gasbag SBS, (b) gasbag SRS, (c) GASBIG hohlraum SBS, and (d) GASBIG hohlraum SRS. The SRS images show that the SRS is well collimated. While the gasbag SBS image shows that the SBS is centered on the lens, that from the GASBIG [Fig. 12(c)] is mostly in a blob that is to one side of the lens. This energy was missed in our earlier (1994) experiments. Figures 12(e) and (f) are more informative, in that they show lineouts through the images and express the result in joules per steradian per incident joule. The lineouts are taken diagonally, such that they pass through the blob in Fig. 12(c). This direction is the radial direction where the center of symmetry is the long axis of the hohlraum. The lineouts show the collimated nature of the SBS and SRS for the gasbag target [Fig. 12(e)]. The GASBIG lineouts in Fig. 12(f) show that although SRS is collimated, the SBS appears about 8° from the beam axis. The appearance of the SBS at such an angle may be due to deflection of the incoming beam as it filaments in the low-density plasma near the laser entrance hole. Filamentation in a plasma that is flowing at near the sound speed can introduce deflection of the beam.[27,28] If after deflection the beam continues to higher density, where direct SBS backscatter is produced, that SBS will not necessarily deflect again on the way out of the hohlraum and so will not retrace its path back out of the hohlraum. Hence there can be a net deflection of SBS that occurs after beam deflection. The direction of the deflection is consistent with the direction of deflection of the forward-propagating beam in x-ray spot motion experiments performed with gas-filled hohlraums.[29]

Figure 13 summarizes the SBS backscattering data for gasbags and GASBIG hohlraums as a function of laser intensity and beam smoothing. Figure 13(a) shows the new SBS data for gasbags; it is noticeable that the backscattering levels are still low and in fact are lower than those observed in 1994 (Fig. 8). One explanation for this is that the time-integrated SBS signal in the earlier experiments was contaminated by stray light or by contributions from short-wavelength SRS. In these newer experiments, we used a diode that (1) was filtered to reject everything but SBS light (near 3ω), (2) had enough time resolution to discriminate against stray light reflected from objects such as the KDP crystal array, within the beam line, and (3) that could be calibrated in a similar manner to the SRS diode. The original motivation for using the diode in place of the calorimeter was that there was a finite reflection from the KDP array that had increased in severity since the first experiments and seemed to vary strongly with crystal tuning. In the 1994 experiments this stray reflection (quantified by observing the calorimeter signal when the beamline was fired with no target present) was small enough to ignore, but with the new experiment it produced random offsets in the signals recorded by the calorimeter. The new diode eliminated this problem and had the side benefit that it was insensitive to any SRS light that would be seen by the SBS calorimeter.

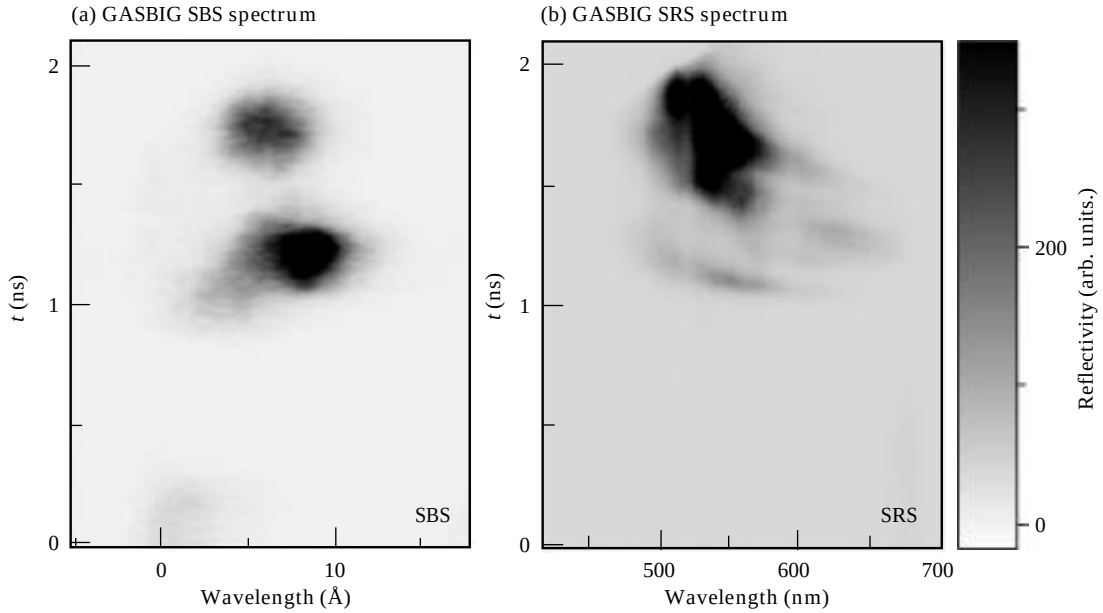

FIGURE 11. GASBIG hohlraum SBS and SRS spectra. (a) Time-resolved SBS spectrum. (b) Time-resolved SRS spectrum; data from FABS direct backscattering diagnostic. (20-07-1095-2444pb01)

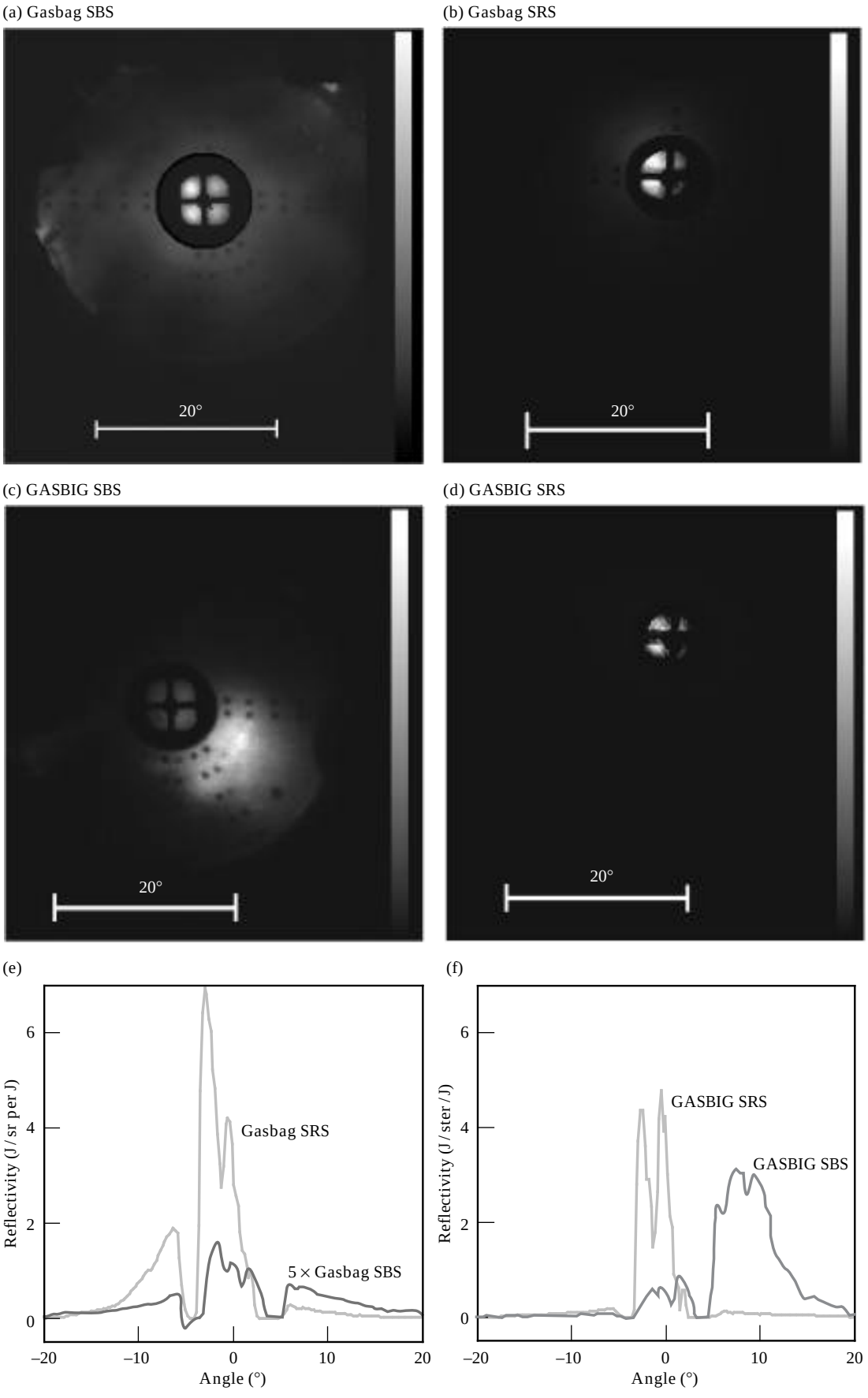

FIGURE 12. Angular distribution of scattered light gasbags and hohlraums. (a) Gasbag SBS; (b) gasbag SRS; (c) GASBIG hohlraum SBS; (d) GASBIG hohlraum SRS; (e), (f) lineouts showing angular dependence of SRS and SBS: (e) gasbag target; (f) GASBIG target. (20-07-1095-2445pb01)

Figure 13(a) shows the peak SBS reflectivity into $f/8$, for the gasbag targets. There has been no attempt to include the contribution due to near-backscattered light. Again, that contribution increases these numbers by a factor of 2 to 3, but the scattered light levels are so low that stray light transmitted by the target striking the NBI plate reduces the precision of the NBI measurement, which then is only good on high-SBS shots. Therefore it is not possible to show the intensity scaling of the data. Figure 13(b) shows similar SBS data for GASBIGS hohlraums; again the NBI contribution has been omitted (the detector malfunctioned on some of the shots), but here the correction factor for the NBI is 6 to 10. In both sets of data it is evident that the addition of SSD reduces the SBS backscattering but that there is no obvious benefit to using four-color smoothing.

Figure 14 summarizes the SRS backscatter data for gasbags and GASBIG hohlraums as a function of laser intensity and beam smoothing. Figure 14(a) shows the data for gasbags. The quantity plotted is the time-resolved SRS reflectivity at the point of maximum plasma temperature (i.e., when the heater beams turn off at 1 ns). The reflectivities for four-color and one-color beam smoothing approach 10% for the NIF intensity of 2×10^{15} W cm^{-2}; the values for experiments that used additional SSD smoothing are closer to 5%. Figure 14(b) shows similar data for the GASBIG hohlraums; the SRS levels at 2×10^{15} W cm^{-2} are similar to those for the gasbag plasmas. The data in both Figs. 14(a) and (b) have had the contributions due to the NBI added and have been scaled to account for energy that would fall into the annulus between 3.6 and 5.3°. These SRS numbers therefore represent the total reflectivity into a cone up to 20° around the beam axis; however (for SRS), most of that energy is within the original $f/8$ solid angle.

The SRS signals are stronger than previously inferred using the FFLEX x-ray technique. An explanation of this discrepancy is that the low phase velocity of electron

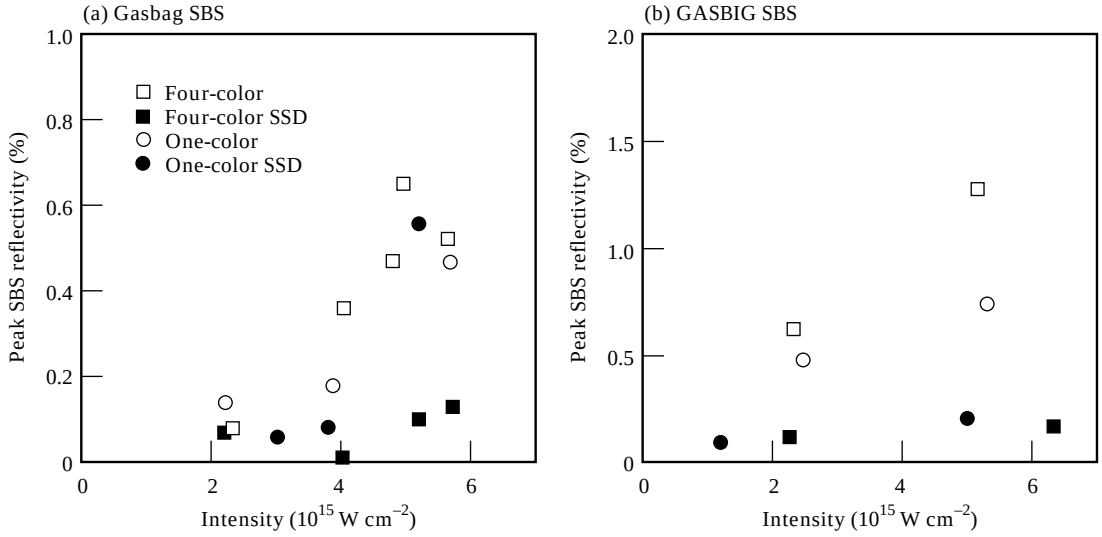

FIGURE 13. SBS vs intensity for various kinds of smoothing. (a) Gasbags. (b) GASBIGS; numbers do not include scattering outside the $f/8$ lens and are the peak reflectivity in time (reflected power/incident power). (20-07-1095-2446pb01)

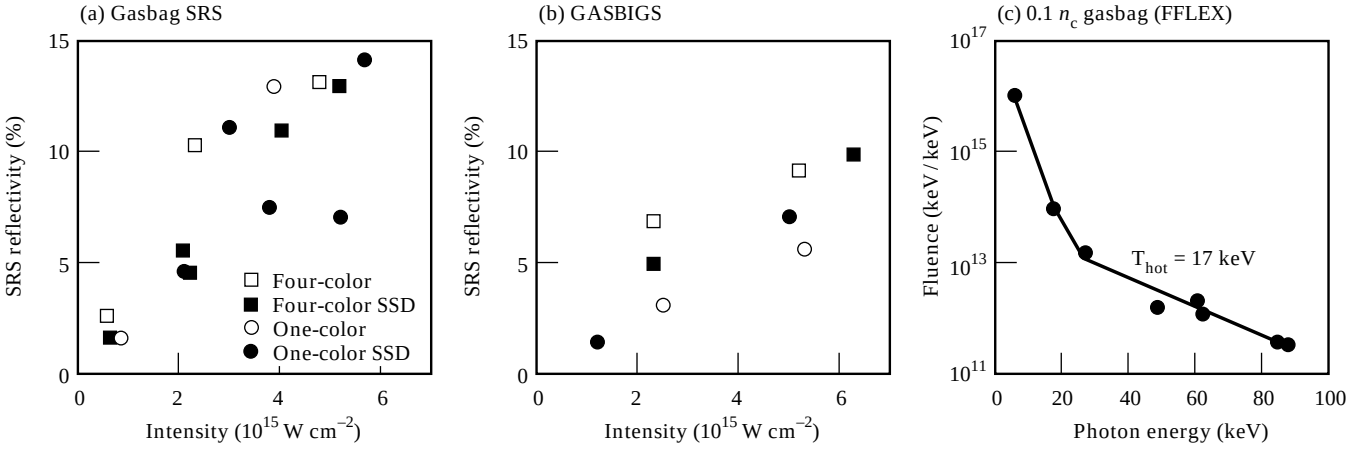

FIGURE 14. SRS vs intensity for various kinds of smoothing. (a) Gasbags; (b) GASBIGS (c) FFLEX data from $0.1n_c$ gasbag. (20-07-1095-2447pb01)

plasma waves in $0.1n_c$ plasma produces low-velocity electrons as the electrons damp the wave. Hence we expect electron energies of 10 to 20 keV to be produced by the SRS that we are detecting. The FFLEX technique is flawed in a gas-filled hohlraum because a significant fraction of any 10-keV electrons will be stopped in the gas (range 400 μm) before they reach the wall. Thus if they produce x rays as they are slowed, it will be through bremsstrahlung resulting from interactions with the lower-Z gas ions rather than with Au. The radiation production scales as Z, so carbon is much less efficient than Au. (The FFLEX analysis requires a knowledge of the Z of the plasma ion.) Even worse, the x rays that are produced cannot then get out of the hohlraum, because the opacity of the Au wall is high for x rays below 40 keV. Hence the FFLEX diagnostic was useful when the fast electrons that were being detected were 100 keV, such as are produced at $0.25n_c$; FFLEX is not useful at the low n_e/n_c encountered in 3ω experiments unless the target has a well-defined Z and has a low opacity to the x rays that are produced. The up side of all this is that 10- to 20-keV electrons are not a preheat threat. The FFLEX is sensitive to electrons that are a preheat threat, because significant quantities of 100-keV electrons could preheat a capsule while 10- to 20-keV electrons would not penetrate the capsule ablator.

Figure 14(c) shows x-ray filter–fluorescer (FFLEX) data from a gasbag shot fired with 10 heater beams (i.e., Beam 7 was also configured as a heater beam, with no RPP or bandwidth and with the same $f/4.3$ focus as the other heater beams) with a total energy of 25 kJ. This setup allowed us to measure the optically scattered SRS on Beam 7 (150 J, 6%) and then (by assuming that all beams were the same) to estimate a total scattered SRS level of 1500 J for the target. The FFLEX data in Fig. 14(c) were fitted to a suprathermal-electron temperature of 17 keV, which is consistent with electrons accelerated by damping of electron plasma waves due to SRS at $0.1n_c$, which is the plasma density expected. The SRS optical spectrum (not shown) peaked at 560 nm, also consistent with $0.1n_c$.

The amount of fast electrons inferred from the spectrum, in Fig. 14(c), is 680 J assuming that the x rays are produced by electrons colliding with the C and H in the C_5H_{12}. Hence the ratio of electron energy to SRS optical light is 1:2.2. The expected division of energy between the electron plasma wave and the scattered light wave at $0.1n_c$ is 1:1.7, implying that there should be 880 J of fast electrons. Although we detected 680 J, our estimate of the energy transferred to the electrons does not take into account ways, other than electron Landau damping, by which energy can be removed from the electron plasma waves. We conclude that the FFLEX provides a useful time-integrated diagnostic of SRS losses if the converting material is known and the target is optically thin to the radiation produced by the electrons. Even in hohlraums, however, the FFLEX is a useful monitor of the electrons (50 to 100 keV) that are capable of preheating the capsule.

As mentioned above, the final test for beam propagation through a NIF plasma is to show that there are no adverse effects to the light that has propagated through such a plasma. Figure 15 shows a summary of the transmitted light from the $f/8$ experiments with gasbag plasmas. The quantity plotted is the time-integrated transmission of the interaction beam through the gasbag. Since the laser light is being absorbed by inverse bremsstrahlung, the transmission at any instant is a function of the temperature and density of the plasma. Using LASNEX-generated density profiles, the expected transmission of the gasbag is 41% for a peak temperature of T_e =3.2 keV and 37% for T_e = 2.8 keV. The transmission values in Fig. 15 are consistent with these numbers for NIF-relevant intensities (up to 2×10^{15} W cm^{-2}) but drop below this value as the intensity is increased above 2×10^{15} W cm^{-2}. Possible explanations for the decrease in transmission at higher intensity are increased losses due to SRS backscattering and spreading of the transmitted beam outside the detector solid angle. The time-integrated SRS for many of the shots above 4×10^{15} W cm^{-2} approached 15%. Adding in losses due to fast electron generation (1/1.7 times the scattered optical energy) results in a total time-integrated "loss" to SRS of order 25% for the higher-intensity shots. This 25% "loss" will reduce the expected transmission to 31% and 28% for peak temperatures of 3.2 and 2.8 keV.

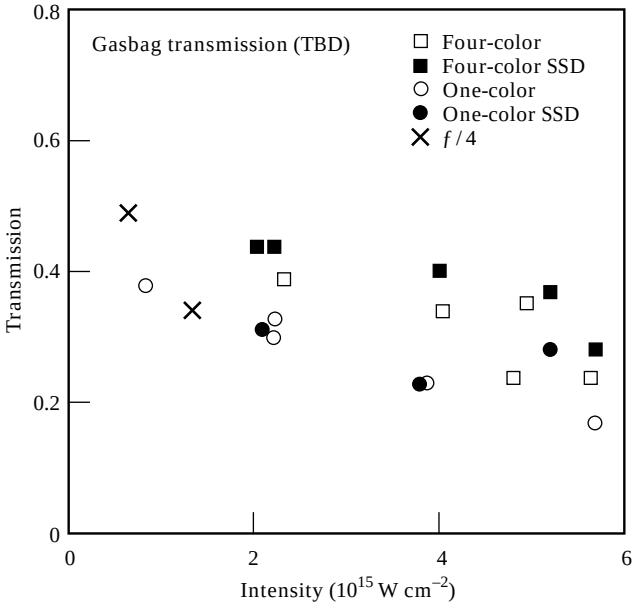

FIGURE 15. Time-integrated transmission of gasbag targets from TBD diagnostic for various kinds of beam smoothing. Expected gasbag transmission is 41% for T_e =3.2 keV and 37% for T_e = 2.8 keV. (20-07-1095-2448pb01)

(The energy put into fast electrons is not really a loss, because the energy will stay in the plasma as the electrons are rapidly thermalized). The time-resolved aspects of these data are still being studied to correlate the SRS and transmitted beam as a function of time.

One interesting aspect of the data shown in Fig. 15 is that the highest transmission is seen in experiments with four-color beam smoothing. This is consistent with four-color smoothing providing better suppression of filamentation and therefore less losses due to parametric processes or beam breakup due to filamentation. However, none of the backscattering data shows any reduction in reflectivity with four-color smoothing. This inconsistency is under study.

A secondary goal of the TBD was to quantify forward Raman scattering. Spectral measurements of forward SRS (400 nm < λ < 900 nm) within 0.2 sr of the probe beam center show spectra that do not appear to depend on the presence of the probe beam. We observe no detectable change in the spectra for similar experiments with the probe beam on or off. The measured spectrum appears to come almost entirely from the sidescattered SRS produced by the heater beams. The level of this sidescattering is about 10 J/sr (wavelength-integrated). We estimate an upper bound on the forward SRS level only from the probe beam to be less than about 5% of the heater beam sidescattering, or about <0.5 J/sr (wavelength-integrated).

Figure 16(a) shows time-integrated backscattered SRS spectra from targets shot with different intensity or beam smoothing. The short-wavelength SRS appears and disappears with changes in the beam smoothing and laser intensity. The lowest intensity case shows very little short-wavelength SRS, while the case with four-color smoothing and 2×10^{15} W cm^{-2} shows significant reflected light at short wavelength. The addition of 1.6 Å of bandwidth reduces the peak reflectivity but also greatly reduces the short-wavelength SRS. Since the short-wavelength SRS is probably associated with low densities in filaments, the above observations are consistent with suppression of filamentation in the lower two curves by low intensity or by SSD. Figure 16(b) shows the results of an F3D calculation of the filamentation of an $f/8$ beam in a $0.1n_c$ plasma at 3 keV. The plot shows the lowest density present within filaments as a function of average laser intensity for four-color smoothing and four-color with additional SSD smoothing. On the axis at right the density is converted to an SRS wavelength assuming 3 keV. The onset of filamentation in F3D occurs at 2×10^{15} W cm^{-2} and correlates with the appearance of the short-wavelength SRS in the data. Hence we may be able to use the short-wavelength SRS as a measure of beam filamentation.

A similar effect is seen in the late-time behavior of the SRS spectra, where the short-wavelength SRS appears as the plasma cools and filamentation thresholds go down. This increase in filamentation sometimes coincides with an increase in the SRS reflectivity, because intensities are higher in filaments, but also the damping of SRS by electron Landau damping is a strong function of temperature near 3 keV (where $k\lambda_D \approx 0.3$). Hence the higher intensities from increased filamentation can conspire with the reduced damping to increase SRS reflectivity as the plasma cools, making time resolved data analysis important.

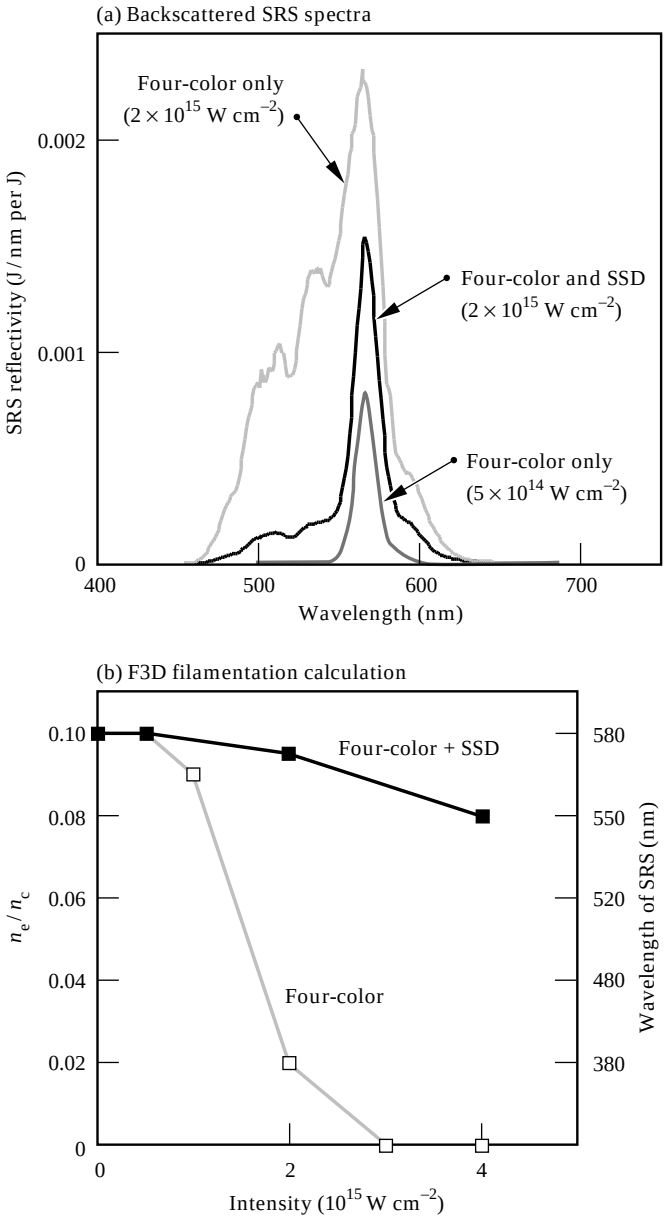

FIGURE 16. (a) Time-integrated backscattered SRS from targets with various intensity or beam smoothing. (b) F3D calculation of filamentation of an $f/8$ beam in a $0.1n_c$ plasma at 3 keV. Plot shows lowest density present within filaments vs average laser intensity for four-color smoothing with and without additional SSD smoothing. (20-07-1095-2449pb01)

Crossed-Beam Experiments

The presence of multiple laser beams with substantial bandwidth in the next generation of ICF experiments will allow a new class of laser–plasma instabilities to take place in which energy from a high-frequency beam is scattered into a low-frequency beam. The mechanisms for these interactions are the same as for the stimulated backscattering instabilities that have been studied for many years in single-color, single-beam experiments. These instabilities grow from plasma wave noise that scatters the incident beam. The interference of the incident and scattered light creates a ponderomotive force on the plasma that reinforces the amplitude of the scattering plasma waves and causes both scattered and plasma waves to grow. The new instability arises when two laser beams cross with different frequency spectra. When the frequencies and crossing angles match, the lower-frequency beam can act as a seed for the sidescattering from the higher-frequency beam. The lower-frequency beam is then amplified by the transfer of energy from the higher-frequency beam. This type of interaction is important both because it can potentially occur near the laser entrance hole of an indirect-drive target and affect the drive symmetry and because it provides an opportunity to study fundamental backscattering processes in experiments in which both the incident and scattered frequencies can be controlled.

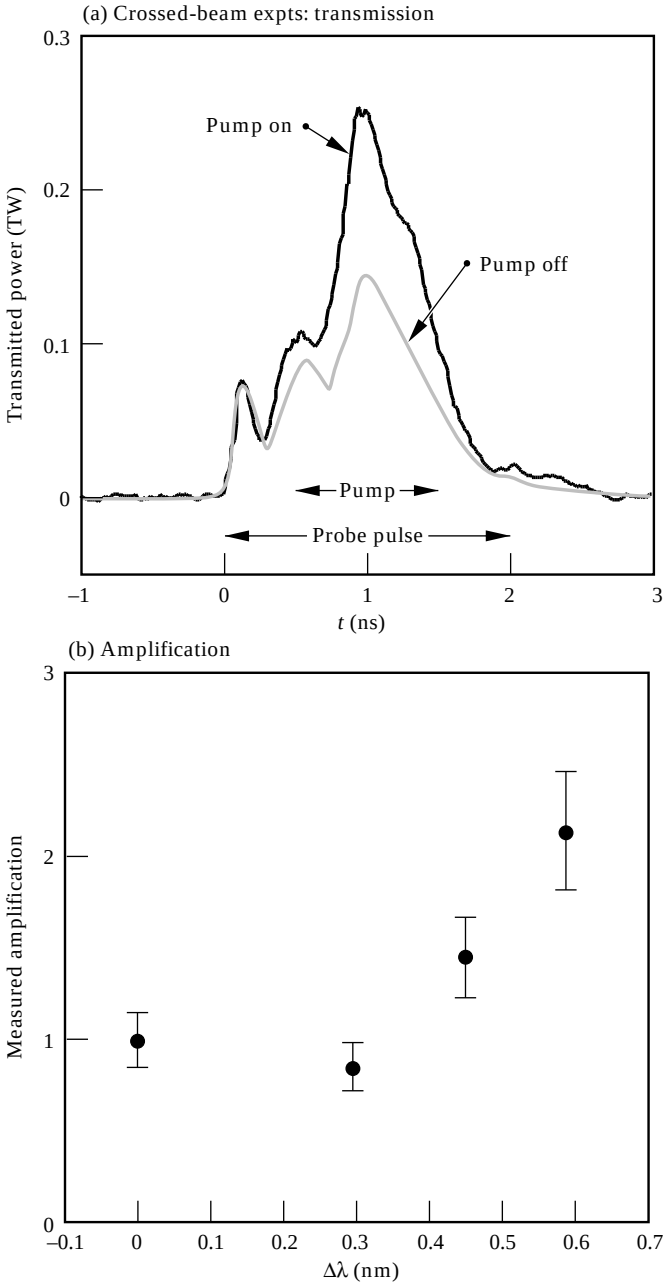

FIGURE 17. Crossed-beam experiments. (a) Typical transmitted light signal; (b) amplification vs tuning of pump with respect to probe beam. (20-07-1095-2450pb01)

Experiments have been carried out at Nova in the past year to study the energy of two beams crossing in a plasma with parameters similar to those expected in NIF hohlraums. The beams cross at a 53° angle and have slightly mismatched frequencies, so that the frequency difference is close to the frequency of the resonant ion-acoustic wave, and Brillouin sidescattering is seeded. The power transmitted through the plasma by the low-frequency probe beam is measured as a function of time by the TBD. The amplification is determined by comparing an experiment in which the high-frequency pump beam is present with one in which it is absent. As shown in Fig. 17(a), the transmitted power rises rapidly after the pump beam is turned on to a value well above what is measured when the pump is off. It has been demonstrated that as much as several hundred joules of energy can be transferred during a 1-ns interaction time, resulting in an amplification of the probe beam by a factor of as much as 2.5. Further, it has been shown that energy transfer occurs only when the difference in the beam frequencies is as large as the frequency of the resonant ion wave, corresponding to $\Delta\lambda = 0.5$ nm in Fig. 17(b). Further experiments are planned to measure the gain vs frequency curve and to directly study the spatial gain rate of Brillouin scattering in laser plasmas for the first time.[30]

Nova Scale-1 Hohlraum Experiments

Most of the diagnostics described above were specifically developed for the long-scalelength plasma experiments, but their larger field of detection made them very useful in other experiments. There is a significant, ongoing effort to understand radiation conversion in gas-filled hohlraums. These experiments use standard “scale-1” Nova hohlraums and a shaped drive pulse that has rapid rise to a “foot” power of ~1 TW / beam, followed by a gradual ramp up to a peak of

about 2 TW / beam at ~1.5 ns. This is the standard PS22 pulse used in the symmetry experiments described in the article "Nova Symmetry: Experiments, Modeling, and Interpretation (HLP3 and HLP4)" on p. 293 of this *Quarterly*. The total pulse duration is ~ 2.2 ns; Fig. 20 shows examples. Measurement of the backscattering from such hohlraums showed that energy loss due to reflection by SBS and SRS played a significant role in determining the hohlraum energetics.

Table 1 summarizes the (time-integrated) backscattering levels observed from the gas-filled hohlraums for various gases and the standard, empty Nova hohlraum. The scale-1 results are all for unsmoothed Nova beams. The quoted reflectivities include contributions from the NBI. For the scale-1 gas-filled hohlraums, the NBI detects a large fraction of the SBS, which appears in a blob similar to that seen with the GASBIG hohlraums [Fig. 12(c)]. The total backscattering losses for gas-filled hohlraums often exceed 15%. Time-resolved measurements show that the peak loss to SBS and SRS combined can be as high as 40% in some targets. LIP calculations of the expected SBS and SRS gain, using plasma conditions from 2-D LASNEX hydrodynamic calculations and average beam intensities, show that although peak gains for SBS are quite high (~30 for both propane- and methane-filled hohlraums), the SRS gain exponents are lower (~20).

TABLE 1. Summary of scattered light levels from NIF-scale and Nova scale-1 hohlraums.

	NIF scale[a]				Nova scale[b]			
	Gasbag		Large hohlraum		Scale-1 hohlraum			
	$0.5–1.0\ 10^{15}$	2×10^{15}	1×10^{15}	2×10^{15}	Au	CH_4	C_3H_8	C_5H_{12}
SBS	<1%	<1%	~0.1%	1.3%	6.5%	9%	11%	4%
SRS	1–2%	4–8%	1.5%	5%	2.5%	5%	12%	14%

[a]All with smoothed "NIF" beam.
[b]All with unsmoothed beams.

The SBS gain exponents calculated for the scale-1 gas-filled hohlraums are similar to or higher than that calculated for the NIF outer beams [Fig. 2(c)] within the Au part of the plasma. Hence in some ways the scale-1 hohlraums let us study that particular problem. The gasbag plasmas mimic the low-*Z* part of the NIF SBS problem, but of course have no plateau of Au to grow SBS at shorter wavelength. The LIP calculations of the SBS gain exponent are shown in Figs. 18(a) and (b) for methane and propane, respectively; both show a peak gain late in time that is red-shifted by 2 to 3 Å from 3ω and corresponds to SBS occurring in the Au shelf that has been ablated from the Au wall by radiative and laser ablation. A time-resolved SBS spectrum from each hohlraum is shown in Figs. 19(a) and (b). The data do not bear much resemblance to the spectral features of the LIP calculations. In particular, the SBS peak sweeps across the spectrum from 8 Å red shifted to 3 Å blue shifted. This feature could be due to SBS growing in the slow-moving Au near the wall at early time. As the pulse intensity ramps up, the point at which SBS grows moves out towards the laser entrance hole, where the faster-moving plasma imposes a blue shift on the scattered light. Such a motion would be consistent with the beam filamenting further out (at lower density) as the intensity ramps up.

The LIP calculations assume a beam intensity spatially averaged in the transverse direction, while the

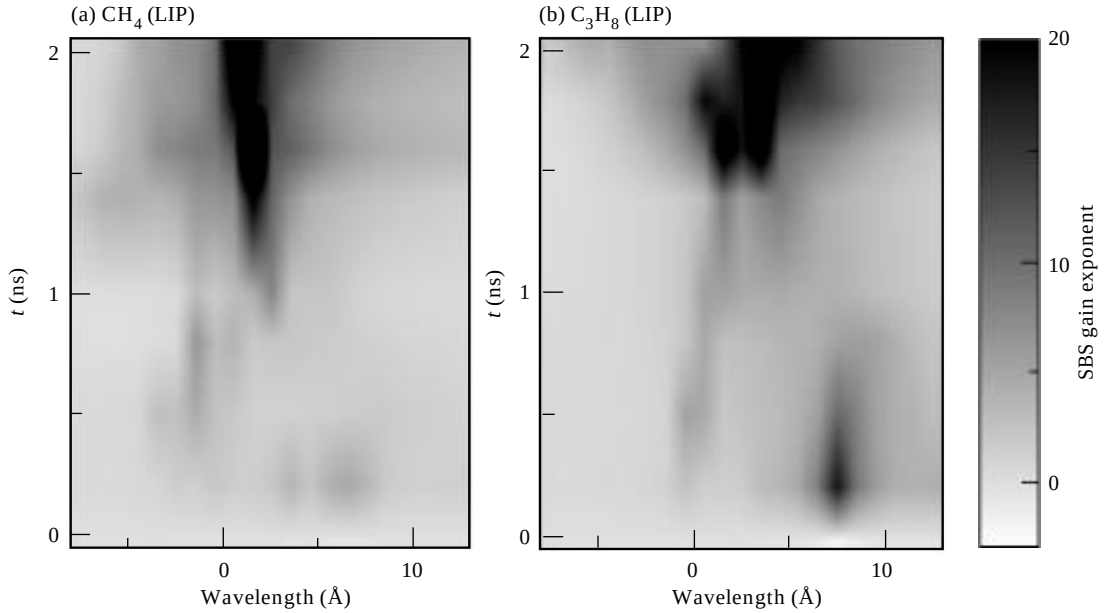

FIGURE 18. Scale-1 hohlraum experiments. (a) LIP gain calculation for a methane-filled scale-1 hohlraum; peak gain exponent is ~30 late in the pulse; (b) LIP calculation for propane; peak gain exponent is ~20 late in the pulse. (20-07-1095-2451pb01)

experiments not only have the short-wavelength speckle structure described earlier but also have longer-wavelength intensity modulations due to the aberration of the Nova beam when it is used without a random phase plate. If we clean up the Nova beam to make it look more like the LIP assumptions, i.e., put on a random phase plate to get rid of the long-wavelength structure and use SSD beam smoothing to reduce the short-wavelength structure, we get the results shown in Figs. 19(c) and 19(d). These figures show the time-resolved SBS spectra from gas-filled hohlraums irradiated with such a smoothed beam. As can be seen by comparing Figs. 18 and 19 for methane and propane, the smoothed-beam data approaches the LIP calculation both in terms of time history and spectral location. The unsmoothed data showed reflected SBS that swept from red shifted to blue shifted as a function of time. The SRS data from these shots (not shown) also showed a significant amount of the SRS coming from low density (~$0.02n_c$), where the LIP calculations showed very low gain exponents. The application of beam smoothing moved the density at which SRS peaked closer to $0.1n_c$, more consistent with the LIP calculations.

The SBS and SRS reflectivity from the scale-1 hohlraums also dropped when beam smoothing was applied. Figure 20 summarizes the time history of the scattered light from the data shown in Fig. 19. For methane, with standard Nova beams [Fig. 20(a)], the SRS and SBS are 6% and 11% respectively; with beam smoothing [Fig. 20(c)], the time-integrated SRS and SBS

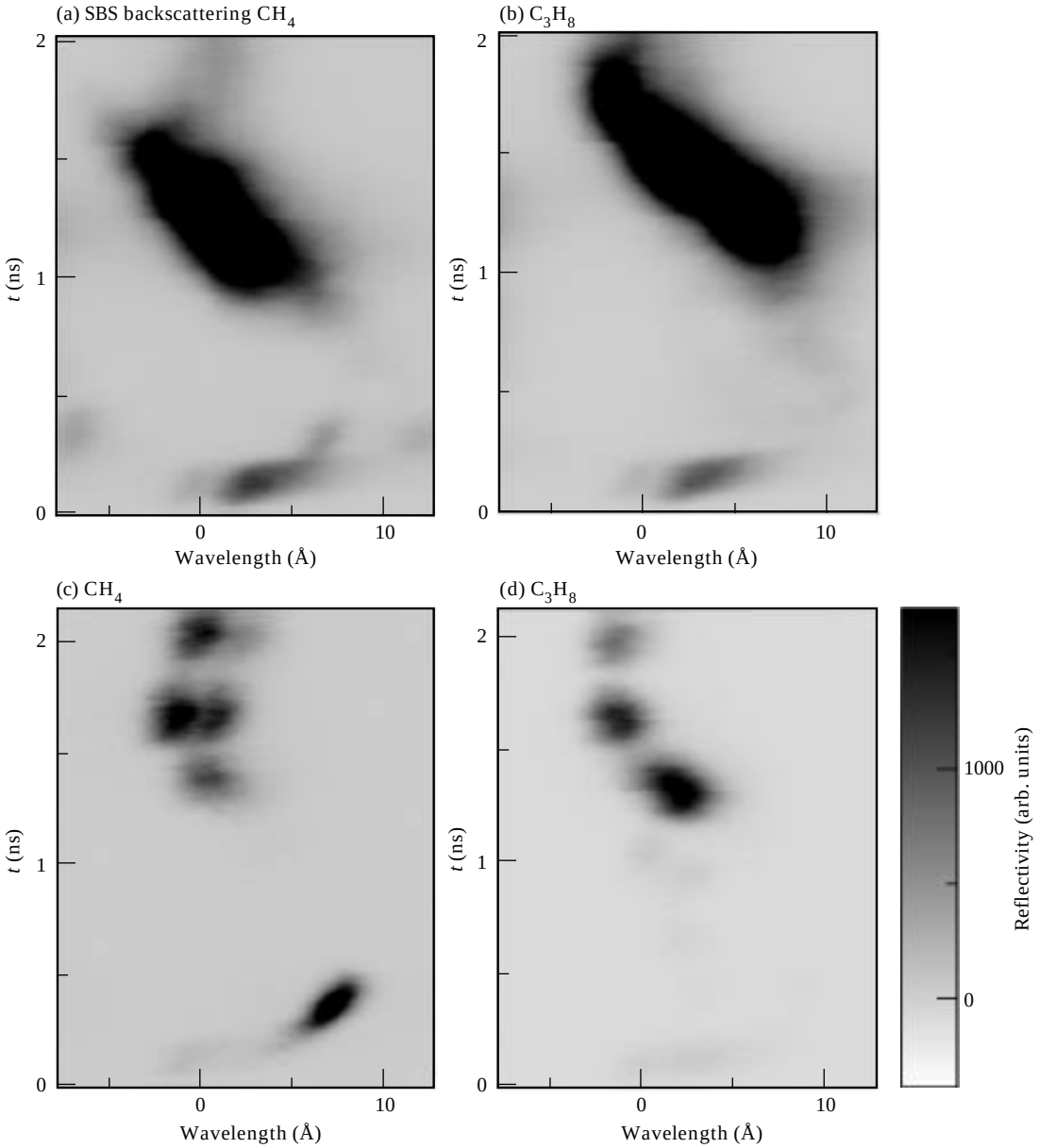

FIGURE 19. Observed SBS backscattering from scale-1 hohlraums. (a) methane-filled; (b) propane-filled; (c) methane-filled, with SSD beam smoothing; (d) propane-filled, with SSD beam smoothing. (20-07-1095-2452pb01)

are 0.1% and 1.4%. For propane the numbers are 11% and 13% before smoothing [Fig. 20(b)] and 1.7% and 1.5% after smoothing Fig. 20(d)] for SRS and SBS, respectively.

These results are encouraging for two reasons:

1. They indicate that if beam smoothing were applied to all ten arms of Nova, we would be able to couple significantly more energy into the gas-filled hohlraums. The implication (which we will explore in future experiments) is that backscattering losses from higher-temperature hohlraums that have higher densities and higher laser intensities may be reduced by smoothing.
2. The fact that the gain in the Au plasma predicted by LIP calculations for scale-1 hohlraums is comparable with that for the NIF outer-beam SBS implies that the smoothed-beam results also apply to the NIF SBS. Note that on the NIF, the beam intensity at the Au wall will be 10^{15} W cm^{-2} [Fig. 1(c)], while in our smoothed-beam hohlraum experiments we have an intensity of 2.5×10^{15} W cm^{-2}. Hence with a smaller target we are mimicking the expected gain exponent on the NIF outer beam in the Au and find that with beam smoothing we can produce low SBS reflectivity.

Conclusion

We have demonstrated that, with appropriate plasma composition and levels of beam smoothing, stimulated scattering in NIF-scale hohlraums can be limited to a few percent for the NIF range of intensities, $I \approx 5 \times 10^{14}$ to 2×10^{15} W cm^{-2}. At this level, stimulated scattering is not expected to have a significant effect on either the energetics or the symmetry of NIF hohlraums. Also, in the NIF intensity range, the light transmitted through the NIF-scale plasmas is consistent with calculations.

Using specially constructed gas-filled plastic balloons and large-scale hohlraums, we have been able to produce plasmas, using 8-9 of Nova's beams, whose density, electron temperature, velocity gradient, and integral interaction path length reproduce the conditions in the low-Z interior of NIF hohlraums. A single Nova beamline was modified to simulate an $f/8$ cluster of four NIF beams in which the wavelength of each beam could differ from that of the others by a few angstroms. Diagnostics were implemented to measure the transmitted laser light and light scattered by SBS and SRS. We measured scattering levels for a variety of smoothing techniques that could be implemented on

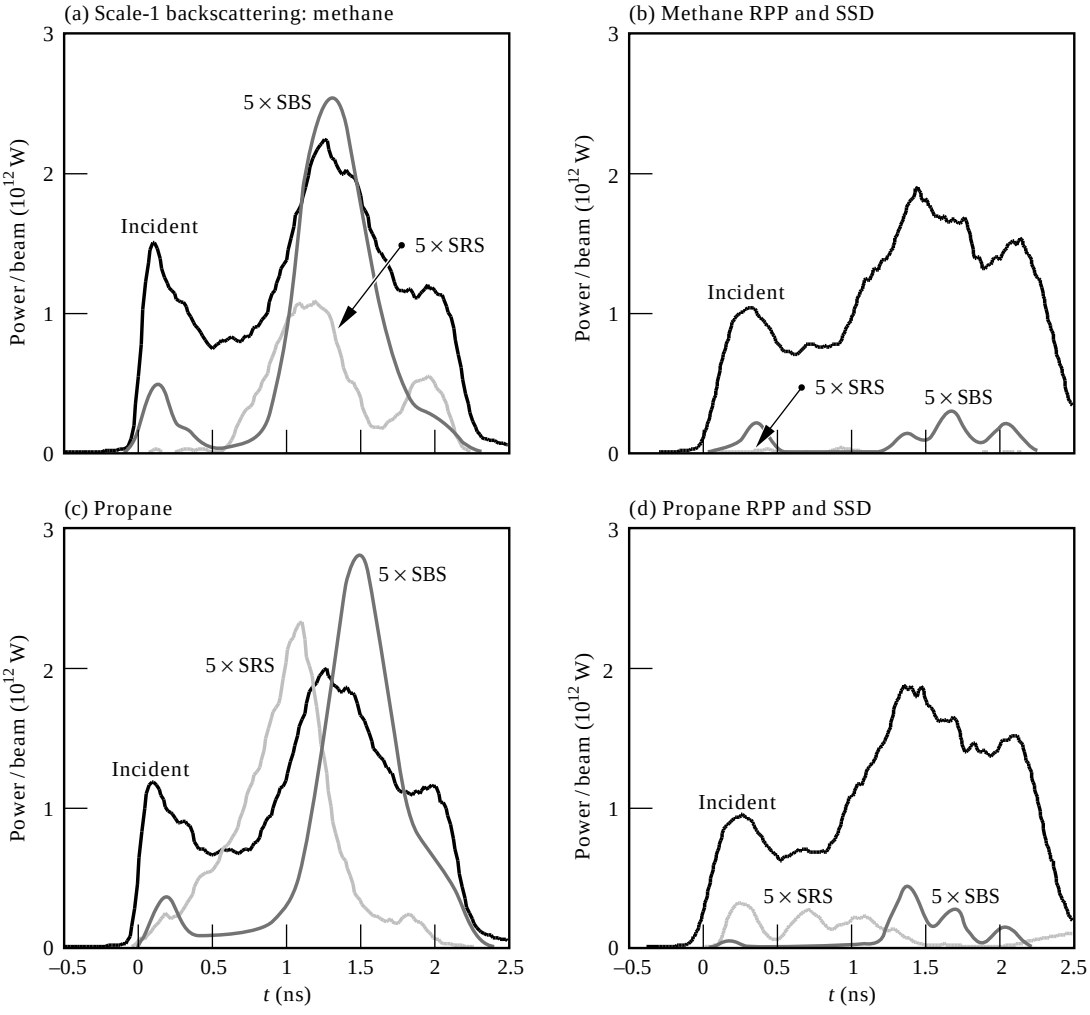

FIGURE 20. Scale-1 hohlraum backscattering pulse shapes. (a) Standard beam conditioning, methane-filled; (b) standard conditioning, propane-filled; (c) SSD, methane-filled; (d) SSD, propane-filled. (20-07-1095-2453pb01)

the NIF, including one- and four-color beams with RPPs only or with 1.6 Å of SSD for temporal smoothing.

For all beam-smoothing schemes and for all intensities of interest to NIF, we find that SBS levels can be limited to ~1% if the ion-acoustic wave is sufficiently damped. This can be achieved by adding hydrogen as a minority species in the low-Z gas fill.

At an intensity of 5×10^{14} W cm^{-2} (the low end of the NIF range), SRS is also limited to a few percent for all smoothing schemes. However, at an intensity of 2×10^{15} W cm^{-2}, near the upper end of the NIF range, SRS is about 10% with RPPs only. With 1.6 Å of SSD, the SRS is limited to about 4 to 5%. With SSD, the frequency spread of SRS is reduced, consistent with theoretical expectations of reduced plasma filamentation with SSD. There appears to be no benefit to having separate frequencies for each of the four beams, with or without SSD. In fact, experiments to explore coupling between beams crossing in the laser entrance hole show that it is possible to transfer energy from one beam to another, potentially affecting hohlraum symmetry, when the frequency difference between beams matches the ion-acoustic frequency.

Although the gasbags and large hohlraums provide a plasma that is a good match to the low-Z interior of a NIF hohlraum, neither reproduces the conditions of a NIF hohlraum near the high-Z wall. The gas balloon has no high-Z wall, and (because of their size) little laser energy reaches the wall in the large hohlraums. However, we find that standard Nova scale-1 hohlraums have conditions in the high-Z wall that are very similar to those of NIF hohlraums. This is because the high-Z conditions are set by inverse bremsstrahlung and x-ray emission and not by the hohlraum scale. Since standard Nova gas-filled hohlraums have a laser intensity comparable to that of the NIF, the inverse bremsstrahlung absorption lengths (of a few hundred micrometers) are also comparable. Although the high-Z shelf is short, it is relatively high density (~$0.2n_c$), has only weak velocity gradients, and has weak Landau damping, so that the gain for SBS can be quite high. Without smoothed beams, SBS levels in Nova gas-filled hohlraums are about 10%, mostly from the Au shelf. As in the case of the low-Z interior, a low-mass minority plasma can provide increased Landau damping to suppress SBS in the high-Z plasma near the wall. We are presently studying this idea, which has application to the NIF. We also find that SBS in the scale-1 hohlraums can be suppressed with sufficient beam smoothing, even without adding a low-Z minority species.

More work remains to be done to fully characterize the range of operating conditions for NIF ignition hohlraums. There would be a substantial benefit if we could extend the range of hohlraum temperatures above that specified for the nominal ignition targets. This would require that hohlraums be operated above the nominal intensity and plasma density range. We have not yet determined the optimum combination of beam smoothing and plasma composition for controlling stimulated scattering, but the techniques examined so far result in low levels of stimulated scattering, and can all be implemented on the NIF.

Notes and References

1. L. J. Suter, A. A. Hauer, L. V. Powers, D. B. Ress, et al., *Phys. Rev. Lett.* 73 (17), 2328–2331; A. Hauer, L. Suter, N. Delameter, D. Ress, et al., *Phys. Plasmas* 2 (6), 2488–2494 (1995).
2. W. L. Kruer, *Phys. Fluids B* 3, 2356 (1991); also "Interaction Physics for Megajoule Laser Targets," in *Laser Interaction and Related Plasma Phenomena,* Vol. 10 (Plenum, New York, 1993), p. 503.
3. See, e.g., M. N. Rosenbluth and R. Z. Sagdeev. *Handbook of Plasma Physics, Volume 3: Physics of Laser Plasma.* A. M. Rubenchik and S. Witkowski, Eds. (Elsevier, Amsterdam, 1991), ch. 9, and references therein.
4. R. L. Berger, B. F. Lasinski, T. B. Kaiser, E. A. Williams, A. B. Langdon, and B. I. Cohen, *Phys. Fluids B* 5, 2243 (1993); R. L. Berger, T. B. Kaiser, B. F. Lasinski, C. W. Still, et al., "Modeling the Effects of Laser-Beam Smoothing on Filamentation and Stimulated Brillouin Scattering," *ICF Quarterly Report* 5 (3), 130, Lawrence Livermore National Laboratory, Livermore, CA, UCRL-LR-105821-95-3 (1995).
5. J. D. Lindl, *Phys. Plasmas* 2 (11), 3933–4024 (Nov. 1995); S. W. Haan, S. M. Pollaine, J. D. Lindl, L. J. Suter, et al., *Phys. Plasmas* 2 (6), 2480–2487 (June 1995).
6. R. L. Berger et al., *Phys. Fluids* 1, 414 (1989).
7. L. V. Powers, R. L. Berger, R. L. Kauffman, B. J. MacGowan, et al., *Phys. Plasmas* 2 (6), 2473 (1985); L. V. Powers, R. L. Berger, D. H. Munro, B. F. Lasinski, et al., *Phys. Rev. Lett.* 74, 2957 (1995).
8. J. Denavit and D. W. Phillion, *Phys. Plasmas* 1, 1971 (1994).
9. M. D. Rosen and J. H. Nuckolls, *Phys. Fluids* 22, 1393 (1979).
10. D. H. Kalantar, B. J. MacGowan, T. P. Bernat, D. E. Klem, et al., *Rev. Sci. Instrum.* 66, 782 (1995); D. H. Kalantar et al., *Phys. Plasmas* 2, 1361 (1995).
11. D. E. Klem, Lawrence Livermore National Laboratory, Livermore, CA, personal communication (1995).
12. R. W. Lee, B. L. Whitten, and R. E. Strout, II, *J. Quant. Spectros. Radiat. Transfer* 32, 91 (1984).
13. J. D. Lindl, "Cairn Hohlraum Scaling Study," in *Laser Program Annual Report—1979,* Lawrence Livermore National Laboratory, Livermore, CA, UCRL-50055-79 (1979), p. 5-80.
14. J. M. Auerbach, K. R. Manes, and D. W. Phillion, "Cairn Scaling Study—The Experiments," in *Laser Program Annual Report—1979,* Lawrence Livermore National Laboratory, Livermore, CA, UCRL-50055-79 (1979), p. 5-62.
15. B. H. Wilde, J. C. Fernandez, W. W. Hsing, J. A. Cobble, et al., "The Design and Characterization of Toroidal-Shaped Nova Hohlraums that Simulate National Ignition Facility Plasma Conditions for Plasma Instability Experiments," presented at the *12th International Conference on Laser Interaction and Related Plasma Phenomena,* Los Alamos National Laboratory, Los Alamos, NM, LA-UR-95-1439 (April 1995), to be published.
16. J. C. Fernandez et al., *Rev. Sci. Instrum.* 66, 626 (1995).
17. R. Kirkwood, J. Moody, and B. MacGowan, "Analysis of Schottky Barrier Diodes for Detection of Pulsed UV Light," Lawrence Livermore National Laboratory, Livermore, CA, internal memorandum (June 1994).

18. Y. Kato, K. Mima, N. Miyanaga, S. Aringa, et al., *Phys. Rev. Lett.* 53, 1057 (1984); H. T. Powell, S. N. Dixit, and M. A. Henesian, *Laser Program Annual Report—1991*, Lawrence Livermore National Laboratory, Livermore, CA, UCRL-LR-105820-91 (1991), pp. 28–38.
19. See National Technical Information Service Document Nos. DE95017671 through DE95017673 and DE95017676 through DE95017700 (J. A. Paisner, E. M. Campbell, and W. J. Hogan, The National Ignition Facility Project, UCRL-JC-117397 and UCRL-PROP-117093, May 1994). Copies may be obtained from the National Technical Information Service, Springfield, VA 22161; D. M. Pennington, *ICF Quarterly Report* 5 (2), 130, Lawrence Livermore National Laboratory, Livermore, CA, UCRL-LR-105821-95-2 (1995).
20. S. Skupsky, R. W. Short, T. Kessler, R. S. Craxton, et al., *J. Appl. Phys.* 66, 3456 (1989).
21. K. Marsh, C. Joshi, and C. McKinstrie, *Bull. Am. Phys. Soc.* 39 (1994).
22. E. A. Williams et al., *Physics of Plasmas. 2,* 1 (1995); H. X. Vu, J. M. Wallace, and B. Bezzerides, *Phys. Plasmas* 1 (11), 3542–3556 (1994).
23. C. E. Clayton, C. Joshi, A. Yasuda, and F. F. Chen, *Phys. Fluids* 24, 2312 (1981).
24. S. C. Wilks, W. L. Kruer, J. Denavit, K. Estabrook, et al., *Phys. Rev. Lett.* 74, 5048 (1995).
25. J. D. Moody, H. A. Baldis, D. S. Montgomery, R. L. Berger, et al., *Phys. Plasmas* 2, 4285 (1995).
26. D. S. Montgomery, J. D. Moody, H. A. Baldis, B. B. Afeyan, et al., "Effects of Laser Beam Smoothing on Stimulated Raman Scattering in Exploding Foil Plasmas," Lawrence Livermore National Laboratory, Livermore, CA, UCRL-JC-123014; submitted to *Phys. Plasmas* (1995).
27. R. W. Short, R. Bingham, and E. A. Williams, *Phys. Fluids* 25 (12), 2302–2303 (1982); D. E. Hinkel, E. A. Williams, R. L. Berger, and L. V. Powers, *Bull. Am. Phys. Soc.* 40 (11) (Oct. 1995), p. 1778 (Annual Meeting of the Division of Plasma Physics).
28. D. F. Dubois and H. A. Rose, *Bull. Am. Phys. Soc.* 40 (11), 1824 (1995); H. A. Rose, *Bull. Am. Phys. Soc.* 40 (11), 1778 (1995).
29. S. G. Glendinning, L. V. Powers, R. L. Kauffman, O. L. Landen, et al., "Measurements of Wall X-Ray Emission Patterns in Gas-Filled Hohlraums," Lawrence Livermore National Laboratory, Livermore, CA, UCRL-JC-123021; to be submitted to *Phys. Rev. Lett.* (1996).
30. R. K. Kirkwood, B. B. Afeyan, W. L. Kruer, B. J. MacGowan, et al., "Observation of Energy Transfer Between Frequency Mismatched Laser Beams in a Large-Scale Plasma," Lawrence Livermore National Laboratory, Livermore, CA, UCRL-JC-122102; submitted to *Phys. Rev. Lett.* (1995).